

Treecode2: The Power of Pluralism. I. Static Tests

Joshua E. Barnes

*Institute for Astronomy, University of Hawaii at Manoa
2680 Woodlawn Drive, Honolulu, HI 96822, USA
barnes@hawaii.edu*

9 February 2026

ABSTRACT

I describe an ‘oct-tree’ N -body code which randomly shifts, reorients, and resizes the root cell at each time step. Averaging over a plurality of root cell positions and orientations statistically restores translational and rotational invariance. The potentials and forces which result can be much more accurate than those obtained from a single force calculation. In this paper, the principle of averaging is tested on static configurations. The next paper will show how this technique can substantially improve global energy, momentum, and angular momentum conservation at a negligible computational cost.

Key words: gravitation – methods: numerical – software: simulations

1 INTRODUCTION

An N -body code designed to simulate the evolution of a collisionless self-gravitating system has two key components. One evaluates the mutual gravitational forces between N particles; the other uses these forces to step the velocities and positions of these particles forward in time.

Large values of N are necessary to accurately represent the distribution functions of collisionless systems. This places a high premium on the computational efficiency of the code. Integrating trajectories is relatively inexpensive; the computing time required scales as $O(N)$, since each particle is handled independently. However, the most accurate and general method of calculating gravitational forces involves evaluating the mutual interactions between all *pairs* of particles. The cost of this *direct-sum* method scales as $O(N^2)$, and for any reasonable value of N it is prohibitive unless special-purpose hardware is available.

Over decades, much effort has been invested in finding faster ways to calculate, if only approximately, the mutual gravitational forces between N particles. Two major types of algorithms have resulted (Binney & Tremaine 2008, Ch. 2.9). *Expansion* methods represent the gravitational potential using a finite number of basis functions; for example, Cartesian particle-mesh codes (e.g. Hockney & Eastwood 1988) use trigonometric functions, while spherical-harmonic codes (e.g. McGlynn 1984; Hernquist & Ostriker 1992) employ multipole expansions. These algorithms treat each particle independently, so their computing costs scale as $O(N)$. But expansion methods have significant constraints; mesh codes have limited resolution, while spherical-harmonic codes can only handle specific problem geometries. Moreover, these schemes may violate galilean invariance; for example, a spherical-harmonic code privileges the origin of the coordinate system, and consequently does not conserve linear momentum.

Hierarchical methods organize the particles into recursively nested regions. This organization is usually represented with a tree structure (Knuth 1973, § 2.3). If the distance between two regions is much greater than the diameter of either, the gravitational field acting on one is insensitive to the details of the mass distribution in the other.

This permits the forces between N particles to be approximated at a cost scaling as $O(N \log N)$ or even $O(N)$ (e.g. Greengard 1990). The accuracy of the resulting forces can be adjusted by user-specified parameters, trading speed for precision. Hierarchical methods can achieve high spatial resolution on arbitrary geometries, circumventing the restrictions of expansion methods.

There are two ways to hierarchically organize the particles. *Lagrangian* methods (Appel 1981, 1985; Jernigan 1985; Porter 1985; Press 1986; Benz et al. 1990) typically adopt binary tree structures, in which each interior node has exactly two descendants. For example, Press (1986) start by finding a pair of mutually nearest neighbors and replacing them by a pseudo-particle representing their centre-of-mass; this process is repeated until only a single pseudo-particle, identified as the ‘root’ of the tree, is left.

In contrast, *Eulerian* methods (Barnes & Hut 1986, hereafter BH86; Greengard & Rokhlin 1987; Dehnen 2000; Stadel 2002) begin by enclosing the particles in a rectangular cell. This root cell is then recursively subdivided, e.g. until each particle is isolated in a separate sub-cell. The most widely used structure, known as an ‘oct-tree’, adopts cubical cells with up to eight descendants (BH86; Greengard & Rokhlin 1987), each describing a separate octant. Oct-tree-codes are relatively easy to implement, lend themselves to at least some level of analysis, and run fairly well on various kinds of hardware.

However, by defining a root cell with a specific position and orientation, Eulerian tree-codes violate translational and rotational invariance. In concrete terms, the outcome of a treecode simulation depends on the position and orientation of the system being simulated; more abstractly, treecode force calculation does not commute with translation or rotation operators. These violations are ‘weak’ in the sense that they can be controlled by adjusting the accuracy parameters, but this always entails a computational cost, and even weak violations of galilean invariance may have consequences.

One such consequence is very easily demonstrated. Consider an isolated system of particles; let m_p and $\mathbf{\tilde{a}}_p$ be the mass and tree-code

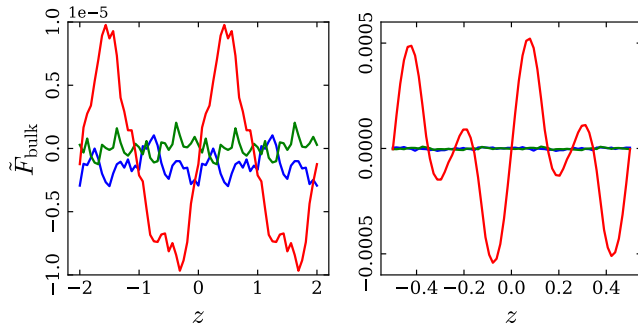


Figure 1. Bulk forces on spherical (left) and disc (right) configurations as functions of position. The sphere is a 3-dimensional Gaussian with unit dispersion, while the disc is generated from the sphere by scaling z coordinates by 0.1; both are realized with $N = 2^{18}$ particles. Tree-code forces are computed with accuracy parameter $\theta = 1$ as each configuration is stepped along the z -axis. Blue, green, and red curves show the bulk forces in the x , y , and z directions, respectively. Note that the vertical range of left-hand plot is $\pm 1.0 \times 10^{-5}$, as indicated by the scaling factor at top, while the range of the right-hand plot is 60 times greater.

acceleration of particle p , and define

$$\tilde{\mathbf{F}}_{\text{bulk}} = \sum_p m_p \tilde{\mathbf{a}}_p, \quad (1)$$

where the sum runs over all particles, to be the net or bulk force on the system. Hernquist (1987) showed that tree-codes conserve linear momentum imperfectly; in other words, $\tilde{\mathbf{F}}_{\text{bulk}}$ does not vanish. This is a result of violating Newton’s third law: the force a single particle exerts on a distant cell is not *exactly* equal and opposite to the force the cell exerts on the particle. Bulk forces *per se* are not a result of violating translational invariance (see § 5). But for an Eulerian code, $\tilde{\mathbf{F}}_{\text{bulk}}$ depends on the *position* of the system within the root cell; force calculation and translation don’t commute.

Fig. 1 illustrates this point. The two examples shown here use a root cell which is centred on the origin and spans from -8 to $+8$ length units along the x , y , and z directions. The left-hand plot shows forces on a unit Gaussian sphere as its centre is shifted from $z = -2$ to $z = 2$; x , y , and z components are shown in blue, green, and red, respectively. All three components vary cyclically; the z component has a much larger amplitude than the other two. Note that the origin an unstable point; positive z displacements yield positive z forces, and vice versa. The plot on the right shows bulk forces on a Gaussian disc with flattening of 0.1 along the z -axis. As the disc translates along its short axis, the maximum force in the z direction is ~ 50 times larger than in the spherical case! Indeed, pure discs simulated with a tree-code sometimes ‘lift off’, perpendicular to their spin plane, unless force calculation is tuned to prioritize accuracy over computing time.

The periodic nature of these forces reflects the structure the oct-tree imposes on the representation of the mass distribution. For example, the trees which result before and after translating the sphere in the left-hand panel of Fig. 1 by 2 length units along the z axis are almost identical; consequently, the force errors which result are very similar.

The issue of momentum conservation has previously been addressed by Dehnen (2000), who introduced an oct-tree algorithm which explicitly symmetrizes gravitational sources and sinks. This strictly enforces Newton’s third law; a single particle and a distant cell interacting with each other will have equal and opposite forces. Moreover, Dehnen’s code achieves $O(N)$ performance by using multipole expansions, instead of lists of interactions, to represent the gravitational field.

The code described here takes a different approach, with the goal of mitigating violations of translational and rotational invariance by averaging over the coordinate systems used to define the tree. The origin, size, and orientation of the root cell are randomly chosen at each successive time-step; each resulting tree provides a different representation of the mass distribution. Individual force calculations still violate invariance, but over time, translational and rotational invariance are statistically recovered. This substantially improves the code’s conservation of energy, linear momentum, and angular momentum. Moreover, force errors largely decorrelate from one timestep to the next, delivering averaged forces which are more accurate than the results of individual force calculations.

A related method was described by Wang et al. (2020), who used cosmological zoom-in simulations with periodic boundary conditions (Springel 2005) to study the formation of extremely low-mass dark haloes. To prevent residual force-calculation errors from corrupting halo formation, they randomly translated the particle configuration within the periodic simulation volume at each timestep (Springel et al. 2021). For periodic boundary conditions, this is equivalent to randomly translating the origin of the oct-tree. Notably, this technique was adopted *in addition* to Dehnen’s algorithm; averaging over random translations offers advantages beyond momentum conservation.

This paper presents static tests of the new force calculation algorithm, deferring a suite of dynamical tests to a sequel (see § 6.1 for a preview). § 2 describes the new code, starting with the rather simple changes needed to implement randomized tree coordinate systems. I also discuss some older modifications which improve the code’s accuracy, efficiency, and robustness. § 3 presents force-calculation tests for a variety of mass distributions, characterizing errors in potential and acceleration, and § 4 shows how averaging can reduce these errors. Discussion and conclusions appear in § 5 and § 6, respectively. A ‘modified’ version (Barnes 1990) of the code, designed to take advantage of special-purpose hardware, is described in an appendix.

2 METHODS

In outline, the new force-calculation algorithm is very similar to the one described by BH86. Given a set of N particles with masses m_p and position vectors \mathbf{r}_p , where p references particles 1, …, N , the code first fits a cubical cell around the system. This cell is then subdivided into eight smaller cells; subdivision continues recursively until each particle is isolated within its own sub-cell. The resulting hierarchy can be represented by a directed graph of ‘nodes’ (cells and particles) in the form of a tree. Each cell directly references (up to) eight nodes, known collectively as the cell’s ‘descendants’; on account of this eight-way branching, this structure is called an ‘oct-tree’.

A typical tree has $O(\log N)$ levels¹, so the computing time required for tree construction is $O(N \log N)$. Each cell’s total mass, centre-of-mass position, and quadrupole moment are computed as part of the construction process.

The gravitational field at any point \mathbf{r} can then be evaluated by a partial recursive scan of the tree, starting from the root cell. Each cell encountered in this process is subject to a simple test (§ 2.3). If it is sufficiently distant from \mathbf{r} , then the field the cell generates is approximated from its mass, position, and quadrupole moment;

¹ Pathological particle distributions can generate much deeper trees, but in practice these do not arise as Monte-Carlo representations of smooth distribution functions.

conversely, if the cell is too close, it is ‘opened’, meaning that each of its immediate descendants is examined instead. Particles which are encountered during the scan are handled as regular two-body interactions. In effect, this procedure approximates the field at \mathbf{r} using a representation of the mass distribution which captures nearby details but becomes increasingly coarse-grained at larger distances. Each level of the tree contributes a bounded number of cells and particles to this representation, so the computing time required to evaluate the field at \mathbf{r} is $O(\log N)$. If forces are required on all N particles, the computing time is $O(N \log N)$. Force calculation is significantly more expensive than tree construction, but both obey the same scaling with N .

2.1 Averaging Algorithm

In the new code, the orientation, scale, and centre of the root cell are chosen randomly. To be specific, let \mathbf{R}_k be a rotation matrix chosen randomly at the k^{th} timestep². Likewise, let S_k be a random scale factor, drawn from a uniform distribution in $\log S_k$ with $|\log S_k| \leq \log S_{\max}$. Finally, let \mathbf{T}_k be a translation vector drawn from a uniform distribution within some maximum radius T_{\max} . Together, \mathbf{R}_k , S_k , and \mathbf{T}_k define an affine transformation³ from the coordinate system (CS) used by the simulation to the one used in building the tree: if \mathbf{r}_p is the simulation position of particle p , its tree coordinate is

$$\mathbf{r}'_p = \mathbf{R}_k S_k (\mathbf{r}_p - \mathbf{T}_k). \quad (2)$$

Tree construction uses the transformed positions \mathbf{r}'_p instead of \mathbf{r}_p . The root cell is centred on the origin of the tree CS; its size is the smallest power of 2 sufficient to enclose all particles. This guarantees that the coordinates of cell centres and boundaries can be accurately represented as binary floating-point numbers; it also implies that setting $S_{\max} = \sqrt{2}$ covers all functionally different possibilities. The resulting tree is very similar to a traditional oct-tree, but organizes particles into a set of cells which are randomly oriented, sized, and positioned with respect to the simulation coordinates. Calculation of cell properties – masses, centre-of-mass positions, and quadrupole moments – can be carried out in simulation coordinates, and force calculation follows the usual hierarchical algorithm.

This technique depends critically on randomizing \mathbf{R}_k , S_k , and \mathbf{T}_k , with no correlation between timesteps. Holding these quantities fixed provides no benefit; it simply replaces one preferred CS with another. But when a *different* tree CS is chosen at each timestep, force errors at timestep k will partly cancel at timestep $k + 1$. Over many timesteps, no CS is preferred, and the algorithm should gradually approach translational and rotational invariance.

2.2 Quadrupole Moments

Following Hernquist (1987), the code uses the quadrupole moments of cells to improve the accuracy of gravity calculations. Consider a cell c containing particles $p \in c$ with masses m_p and positions \mathbf{r}_p ; the cell has total mass m_c and centre of mass position \mathbf{r}_c . Let

² Strictly speaking, the static tests presented here do not employ timesteps; k is simply an integer. The timestep terminology is used to simplify the description.

³ Eq. (2) preserves angles, ensuring that cubes are cubes. Non-cubical cells tend to have large high-order moments, which may require octapole or higher corrections.

$\mathbf{s}_p = \mathbf{r}_p - \mathbf{r}_c$ be the position of particle p relative to the cell’s centre of mass; then the cell’s traceless quadrupole moment is

$$\mathbf{Q}_c = \sum_{p \in c} m_p (3 \mathbf{s}_p \otimes \mathbf{s}_p - s_p^2 \mathbf{I}), \quad (3)$$

where \mathbf{I} is the identity matrix. The cell’s gravitational potential at position $\mathbf{r} = \mathbf{s} + \mathbf{r}_c$ can then be expanded to quadrupole order:

$$\phi_c(\mathbf{s}) \simeq -\frac{G m_c}{s} - \frac{G \mathbf{s} \cdot \mathbf{Q}_c \cdot \mathbf{s}}{2s^5}. \quad (4)$$

This expression should be modified to include Plummer softening (Aarseth 1963). In the limiting case where c contains a single particle, so that all higher-order moments vanish, the softened potential is

$$\phi_c(\mathbf{s}) = -\frac{G m_c}{(s^2 + \epsilon^2)^{1/2}}, \quad (5)$$

where ϵ is the softening length. By analogy, Hernquist (1987) implemented softening by replacing s with $(s^2 + \epsilon^2)^{1/2}$ in the denominators of *both* terms in eq. (4). This gives acceptable results in the small- ϵ limit, but is somewhat less accurate in situations where large amounts of mass are concentrated on scales of order ϵ (Barnes 2012).

A better approximation to the softened quadrupole potential was suggested by Keigo Nitadori (personal communication, 2015):

$$\phi_c(\mathbf{s}) \simeq -\frac{G m_c}{(s^2 + \epsilon^2)^{1/2}} - \frac{G (\mathbf{s} \cdot \mathbf{Q}_c \cdot \mathbf{s} - \epsilon^2 \tilde{\mathbf{Q}}_c)}{2(s^2 + \epsilon^2)^{5/2}}, \quad (6)$$

where

$$\tilde{\mathbf{Q}}_c = \sum_{p \in c} m_p s_p^2. \quad (7)$$

This approximation substantially improves the accuracy of softened body-cell interactions, while imposing only a modest computational cost. It is implemented as a compile-time option.

The acceleration due to the cell is $\mathbf{a}_c = -\partial \phi_c / \partial \mathbf{r}$.

2.3 Opening Criteria

To decide if a cell c is so close to a particle p that it *must* be opened, BH86 used a simple geometrical test. Let $s = |\mathbf{r}_p - \mathbf{r}_c|$ be the distance between p and c , and let ℓ_c be the edge-length of c . Then c must be opened if

$$s < \ell_c / \theta, \quad (8)$$

where θ is a parameter, of order unity, which controls the accuracy of the force calculation. In principle, this geometrical criterion insures that the maximum relative error from any individual cell is bounded (e.g., Barnes & Hut 1989). This test can be implemented very efficiently; the value of $(\ell_c / \theta)^2$ is stored in each cell during tree construction, and can be quickly compared to s^2 for every cell encountered during a recursive tree scan.

In practice, this simple criterion can fail if the centre-of-mass (CM) of a cell is far from its geometric centre. For example, if the CM lies in one corner of c and p lies at the opposite corner, then eq. (8) will fail unless the parameter $\theta < 1/\sqrt{3} \simeq 0.577$. Noticing this, Hernquist (1987) considered an additional test to make sure that c does not contain p , although experiments with a limited set of particle distributions suggested this was unnecessary provided that $\theta \lesssim 1.2$. Subsequently, however, Salmon & Warren (1994) showed that eq. (8) could fail catastrophically for $\theta \sim 1$ if p is replaced with a compact, gravitationally bound system of particles; in this situation, interactions within the bound system are not evaluated, resulting in the ‘detonating satellite’ phenomenon.

To cure this problem, I take the offset d_c between c 's geometric centre and its CM into account (Barnes 1994). Eq. 8 is replaced with

$$s < \ell_c / \theta + d_c. \quad (9)$$

This criterion positively guarantees that any cell which contains p will be opened provided that $\theta < 2/\sqrt{3} \approx 1.16$, which is larger than the θ values typically employed. Heuristically, eq. (9) gives ‘extra attention’ to cells which have large offsets d_c relative to their sizes; this seems reasonable since such cells are likely to have significant high-order moments. The new code uses eq. (9), although the original criterion is available as a run-time option.

Any tree scan which correctly opens every cell containing particle p will *necessarily* visit p itself. This provides a simple check which is easily implemented in the force-calculation tree scan. By default, a tree scan which fails this test triggers a fatal error.

2.4 Threading the Tree

Since force calculation entails performing many tree scans, it is important to make tree traversal as efficient as possible. During construction, each cell of the tree stores the addresses of its immediate descendants in an ordered array. The resulting data-structure can only be traversed by a recursive algorithm, or equivalently, by an iterative algorithm which maintains an explicit stack of tree nodes (particles and cells) to process. This imposes a significant overhead on each tree scan. But as Makino (1990a) noted, a straightforward transformation permits the tree to be scanned with a simple iterative algorithm.

The basic idea of Makino’s transformation is familiar to anyone who has perused a hierarchically-structured document. Each page of information offers two hyperlinks: one goes to a page which discusses the *next* topic, while the other (which is optional) goes to a page or pages which discuss the present topic in *more* detail.

Algorithm 1 presents the iterative tree scan. Here n is either a cell or a particle, and s is a flag which indicates if the scan has correctly visited p . Each cell c stores two pointers: $\text{Next}(c)$ is the node to be visited if c does not need to be opened, while $\text{More}(c)$ is the first descendent of c . Each particle p just stores one pointer, $\text{Next}(p)$. The constant ROOT is the root cell of the tree, and NULL is a sentinel value marking the end of the tree. The function $\text{IsCell}(n)$ is true if n is a cell, and $\text{MustOpen}(n, p)$ implements the test in eq. (9).

The tree is threaded with Next and More pointers following the initial phase of tree construction. Once the tree is threaded, the eight descendent pointers of a cell are no longer needed, and the memory they occupy can be reused, in particular, for quadrupole moments.

In passing, it’s worth mentioning that the Next pointer is also useful during the initial phase of tree construction. On occasion, two particles may have *exactly* the same positions, at least to 32-bit precision⁴. This situation is easily detected as particles are inserted into the tree structure; if it occurs, the second particle is linked after the first using the Next pointer. This linkage is preserved when the tree is threaded.

3 STATIC TESTS

While the value of tree averaging should ultimately be demonstrated by fully dynamical simulations (Paper II), the results of such simulations are hard to interpret without a good understanding of the errors

⁴ This typically arises when a system with a high central density, such as a Jaffe (1983) model, is displaced a few scale lengths from the origin.

Algorithm 1 Force calculation for particle p by iterative tree scan.

```

 $n \leftarrow \text{ROOT}$ 
 $s \leftarrow \text{FALSE}$ 
while  $n \neq \text{NULL}$  do
  if  $\text{IsCell}(n)$  then
    if  $\text{MustOpen}(n, p)$  then
       $n \leftarrow \text{More}(n)$ 
    else
      process interaction of  $p$  with cell  $n$ 
       $n \leftarrow \text{Next}(n)$ 
    end if
  else
    if  $n \neq p$  then
      process interaction of  $p$  with particle  $n$ 
    else
       $s \leftarrow \text{TRUE}$ 
    end if
     $n \leftarrow \text{Next}(n)$ 
  end if
end while
if  $s \neq \text{TRUE}$  then
  error: scan did not visit  $p$ 
end if

```

arising at each time step. Therefore, this paper presents tests using static configurations. The test procedure is described in § 3.1. I then examine errors in force calculations for individual particles (§ 3.2), error distributions for all particles (§ 3.3), trends with opening angle (§ 3.4), the origin of bulk forces and torques (§ 3.5 and 3.6), and computing times (§ 3.7). In these tests, I employ a single tree CS, replacing eq. (2) with $\mathbf{r}'_p = \mathbf{r}_p$. The goal here is to establish a baseline with which to evaluate the effects of tree averaging.

An emerging theme of this study is that tree-code force errors are *not statistically independent*. This is not a new observation (e.g., Barnes & Hut 1989), but its implications have not always been recognized. An understanding of error correlations is valuable in interpreting tree-code results.

3.1 Test Procedure

The particle configurations used to test the algorithm are naturally organized into a $5 \times 5 \times 5$ array. The first dimension of this array selects one of five different mass models. The second dimension fixes the number of particles used to realize each model, ranging in multiplicative steps of 4 from $N = 2^{14} = 16384$ to $N = 2^{22} = 4194304$ (using powers of two for N helps ensure that particle masses and their sums are accurately represented as floating point numbers). The third dimension specifies a unique random number seed used when constructing each specific realization. The five realizations constructed for each choice of mass model and N are statistically equivalent to each other; by comparing results across an ensemble of realizations, one can gain some idea of statistical uncertainties.

The five mass models include three spherical systems with different density profiles, a flattened disc, and a small group of spherical systems, as follows:

- (i) A Hernquist (1990) model, with mass $M = 1$ and scale radius $a = 1$. The density profile is smoothly tapered at radius $b = 100$ (Barnes 2012). The model is offset from the origin by a random vector \mathbf{r}_{off} drawn from a uniform distribution, with magnitude $|\mathbf{r}_{\text{off}}| \leq 4$ length units.
- (ii) A Jaffe (1983) model, with mass $M = 1$ and scale radius

$a = 1$. The density profile is smoothly tapered at radius $b = 100$. The model is randomly offset.

(iii) An [Einasto \(1965\)](#) model, with mass $M = 1$, half-mass radius $r_h = 1$ and index $n = 3.5$. The model is randomly offset.

(iv) A flattened disc, with mass $M = 1$, generated by drawing coordinates (x_p, y_p, z_p) from a unit Gaussian, and then rescaling $z_p \rightarrow 0.1z_p$. The disc is randomly offset *and* rotated.

(v) A group of 4 [Einasto \(1965\)](#) models, each generated with $N/4$ particles, and offset to positions chosen at random within a sphere of radius 4.

Random offsets and/or rotations are used to examine how the tree-code behaves when the distribution of particles is not aligned with the coordinate system. Again, a different seed was used each time these were chosen.

A mass model with density $\rho(\mathbf{r})$ is realized by choosing N positions \mathbf{r}_p , where p labels particles $1, \dots, N$. The chance of choosing position \mathbf{r} is directly proportional to $\rho(\mathbf{r})$; consistent with this strategy, each particle has equal mass $m_p = M/N$. Positions are drawn independently, so the number of particles in any given volume obeys Poisson statistics. This gives rise to ‘microscopic’ differences between the configurations in a given ensemble; in contrast, the random offsets and/or rotations introduce ‘macroscopic’ differences.

For each realization, I first computed reference forces and potentials via a simple direct-sum algorithm, setting $G = 1$ and using Plummer softening with $\epsilon = 0.01$. Direct-sum forces take an excessively long time to evaluate for $N > 2^{20}$, so for realizations with $N = 2^{22}$, I computed forces on a subset of 2^{18} particles which uniformly sample the full system. Let ϕ_p and \mathbf{a}_p be the resulting potential and acceleration for particle p . These quantities were computed in double precision to avoid roundoff issues with sums of $O(N)$ terms.

I then used the tree-code to compute approximate potentials $\tilde{\phi}_p$ and accelerations $\tilde{\mathbf{a}}_p$ for each particle p in all 125 realizations. By default, all test calculations included quadrupole moments (results obtained without them are briefly discussed in § 3.4). Forces were calculated for 7 opening-angle values equally spaced from $\theta = 0.4$ to 1.0, using the same set of realizations for each. This strategy introduces a subtle complication: a realization which happens to be an outlier for one θ value is often an outlier for other values as well. It would have been cleaner to use a unique set of realizations for each θ value, but the direct-sum forces were too expensive. Single precision was adequate for this range of θ values, since each sum contains only $O(\log N)$ terms.

The basic quantities of interest are the net or absolute potential and acceleration errors for particle p :

$$\Delta\tilde{\phi}_p \equiv \tilde{\phi}_p - \phi_p, \quad \Delta\tilde{\mathbf{a}}_p \equiv \tilde{\mathbf{a}}_p - \mathbf{a}_p. \quad (10)$$

3.2 Single Particles

A tree-code approximates the potential and acceleration of particle p by summing its interactions with a set P_p of particles and another set C_p of cells (eq. 6). The former are, by definition, accurate, but each of the latter is an approximation which introduces some error. Let $\tilde{\phi}_{p,c}$ and $\tilde{\mathbf{a}}_{p,c}$ be tree-code approximations for the potential and acceleration of cell c , while $\phi_{p,c}$ and $\mathbf{a}_{p,c}$ are computed by direct-sum over all particles in c . Then the errors for cell c are $\Delta\tilde{\phi}_{p,c} \equiv \tilde{\phi}_{p,c} - \phi_{p,c}$ and $\Delta\tilde{\mathbf{a}}_{p,c} \equiv \tilde{\mathbf{a}}_{p,c} - \mathbf{a}_{p,c}$. These cell-by-cell errors can be summed to obtain the absolute errors:

$$\Delta\tilde{\phi}_p = \sum_{c \in C_p} \Delta\tilde{\phi}_{p,c}, \quad \Delta\tilde{\mathbf{a}}_p = \sum_{c \in C_p} \Delta\tilde{\mathbf{a}}_{p,c}. \quad (11)$$

The sums in eq. (11) can be visualized as quasi-random walks.

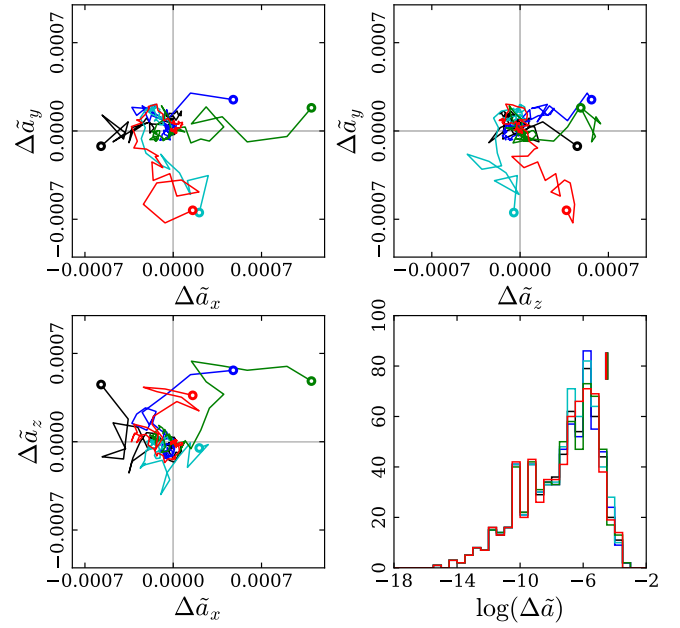


Figure 2. Acceleration errors for single particles, plotted as quasi-random walks. Five particles were sampled from radius $r \simeq 1$ in a Hernquist model; each is plotted in a different color. The model has $N = 2^{18}$ particles, and forces were computed with $\theta = 1.0$. Top left, top right, and bottom left panels show projections of acceleration errors on the (x, y) , (z, y) , and (x, z) planes, respectively. Steps are ordered from smallest to largest in length; an open circle marks the end of each walk. Bottom right panel shows error distributions; vertical marks indicate RMS values of $\Delta a_{p,c}$.

Fig. 2 presents examples of $\Delta\tilde{\mathbf{a}}_p$ for a Hernquist model with $N = 2^{18} = 262144$, computed using $\theta = 1.0$. There’s no natural order to the set C_p , so in these plots the steps are ordered by increasing $|\Delta\tilde{\mathbf{a}}_{p,c}|$.

All of these random walks are dominated by their largest steps. In the three orthogonal views of the acceleration errors, a handful of steps at the end account for most of the displacement from the origin. The distributions of $\log |\Delta\tilde{\mathbf{a}}_{p,c}|$ plotted in the lower right panel support this; the vast majority of cells each particle interacts with generate numerically small errors, while a tiny minority yield large errors. Although the cell-opening criterion limits the *relative* errors of cells in eq. (11), there is no corresponding bound on the *absolute* error. It’s not unusual for the total gravitational force at a given point to be dominated by a relatively small number of cells – indeed, that’s basically the point of a tree-code! The relative errors due to these dominant cells are typical, but their absolute errors are still large.

Close inspection of Fig. 2 hints that acceleration errors due to different cells are *correlated* with each other. None of these paths are linear, but most of them seem to make fairly consistent progress away from the origin as they reach their terminal points. However, the very uneven distribution of step lengths makes it difficult to be certain.

Correlations are obvious in Fig. 3, which plots acceleration errors for the Gaussian disc used in Fig. 1. Here, the disc was positioned at the origin, and forces for a sample of five particles drawn from $\sqrt{x^2 + y^2} < 0.2$ and $z \simeq 0.15$ are plotted. While individual steps retain substantial random components, all five paths are clearly biased in the positive z direction, and this is reflected in steps of all

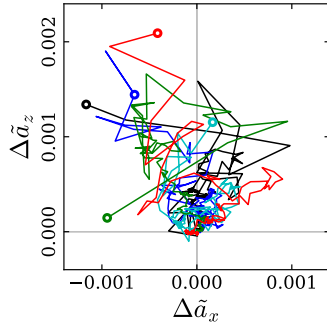


Figure 3. Acceleration errors for single particles from a disc model. Five particles were sampled from $\sqrt{x^2 + y^2} < 0.2$ and $z \approx 0.15$. Other details as for Fig. 2

sizes. Tree-codes systematically underestimate the vertical acceleration fields of thin discs. This bias arises because highly stratified mass distributions generate cells with significant octapole and higher (hereafter ‘octapole-plus’) moments, which are excluded when cell fields are truncated at quadrupole order (§ 2.2).

3.3 Error Distributions

The absolute errors $\Delta\tilde{\phi}_p$ and $\Delta\tilde{a}_p$ for particle p are fundamental quantities, but in many cases it’s useful to discuss the corresponding normalized or *relative* errors,

$$\delta\tilde{\phi}_p \equiv \Delta\tilde{\phi}_p/|\phi_p|, \quad \delta\tilde{a}_p \equiv |\Delta\tilde{a}_p|/|\mathbf{a}_p|. \quad (12)$$

Relative errors simplify comparison of results from different models, and relative acceleration errors are more relevant in determining the accuracy of particle trajectories. Note, however, that particles at the very centre of a model may yield alarmingly large values of $\delta\tilde{a}_p$, since the normalizing acceleration $|\mathbf{a}_p|$ can be very small.

Fig. 4 presents scatter-plots of relative errors in potential and acceleration. For the three spherical models, the horizontal axis shows the distance $\hat{r}_p = |\mathbf{r}_p - \mathbf{r}_{\text{off}}|$ from the system’s centre, while for the disc model, the cylindrical radius \hat{R}_p is used instead. The group model has no unique centre, so the horizontal axis shows the potential ϕ_p . Each realization of $N = 2^{18}$ particles is represented by two panels: the upper one shows the relative potential error $\delta\tilde{\phi}_p$, which must be plotted on a linear scale, and the lower one shows the relative acceleration error $\delta\tilde{a}_p$, plotted on a logarithmic scale. The softening length was $\epsilon = 0.01$. Tree-code potentials and accelerations were calculated using an opening angle $\theta = 0.8$; cell potentials include softening-corrected quadrupole terms (eq. 6). Unless otherwise stated, these parameters are used in all subsequent force-calculation plots.

The errors for the three spherical models all display broadly similar patterns. In general, the structure of the errors reflects the underlying oct-tree; the ‘barbs’ in the $\delta\tilde{\phi}_p$ distributions are often spaced by factors of 2 in \hat{r}_p . This also appears in the ‘sawtooth’ pattern of acceleration errors $\log_{10} \delta\tilde{a}_p$, along with a general increase toward the centre of each model. At first glance, potential errors may appear symmetric about $\delta\phi = 0$, but a second look corrects this impression; the Jaffe model (top row, second panel) provides a particularly clear example of asymmetry, with $\tilde{\phi}_p > \phi_p$ everywhere within $\log_{10} \hat{r} < -2$.

Errors for the disc and group models paint a different picture. They are significantly larger than those typical of spherical models. The fairly orderly structures of $\delta\tilde{\phi}_p$ versus \hat{r}_p seen in the spherical cases are replaced with much more chaotic patterns. Acceleration errors generally increase toward the centre of the disc, or deeper within the

potential well of the group, but have wide distributions everywhere. Potential errors are not symmetrically distributed about $\delta\tilde{\phi} = 0$, with $\tilde{\phi}_p$ overestimated in some places, and underestimated in others.

These scatter-plots display just one realization for each model. Do the other four ensemble members, each with its own offset, orientation (for the disc model), layout (for the group model), and Monte-Carlo sampling, yield similar results? Fig. 5 plots histograms of relative errors in potential $\delta\tilde{\phi}_p$ and acceleration $\log_{10} \delta\tilde{a}_p$ for all five mass models. Each realization is represented by a different color to help show variations within each ensemble.

The Hernquist model (top row) yields distributions of $\delta\tilde{\phi}$ which are nearly symmetric around zero, with only modest variations between configurations. Most of the variation is driven by random offsets; Monte-Carlo sampling plays a much smaller role. In particular, the realization represented by the green histograms is situated in a ‘sweet spot’ with respect to the oct-tree. As a result, its $\delta\tilde{\phi}$ distribution (left panel) is narrower and more peaked than the others; moreover, its $\log_{10} \delta\tilde{a}$ distribution (right panel) is shifted toward smaller values.

These sweet spots – offsets which yield atypically accurate potentials and forces – are observed with all three spherical mass models, although none of the other realizations shown in Fig. 5 happens to fall near one. One such spot always lies at the origin (zero offset: $\mathbf{r}_{\text{off}} = (0, 0, 0)$), but similar results arise with other offsets as well. In Fig. 5, the realization giving rise to the green histograms had an offset of $\mathbf{r}_{\text{off}} = (-0.155, -0.207, -3.935)$, adjacent to a sweet spot at $\mathbf{r}_{\text{off}} = (0, 0, 4)$. In general, it appears that sweet spots result when the bulk of the mass distribution is more or less evenly divided between eight cells (which need not all be siblings).

In contrast, the disc models (fourth row) yield $\delta\tilde{\phi}$ distributions which vary widely and are manifestly *asymmetric* about 0. The potential and acceleration errors are substantially larger than those found for spherical systems, consistent with Fig. 4. Again, most of the variation among the ensemble members arises because of macroscopic differences in disc orientation and position, as opposed to microscopic differences in Monte-Carlo sampling. The disc represented by the red histograms, which happens to be tilted by only $\sim 5.3^\circ$ with respect to the x - z plane, yields significantly more accurate potentials and accelerations compared to other ensemble members. This is a further consequence of singling out a specific coordinate system: discs which are aligned with the coordinate planes of the tree are handled more accurately. Thus, in addition to sweet spots, flattened systems also have ‘sweet orientations’.

The group realizations yield fairly narrow $\delta\tilde{\phi}$ distributions – indeed, they somewhat narrower and more symmetric than the distributions for the Einasto models making up these groups. These distributions display noticeable variations arising from the random construction of each realization. However, these variations are not reflected in the $\delta\tilde{a}$ histograms, which seem remarkably consistent. The acceleration errors are only slightly larger than those obtained for individual Einasto models.

3.4 Errors vs. Opening Angle

How do potential and acceleration errors depend on the opening angle? To address this question, it helps to quantify the overall errors of a force calculation with a few key numbers:

$$\begin{aligned} \delta\tilde{\phi}_{\text{avg}} &\equiv \frac{1}{N} \sum_p \delta\tilde{\phi}_p, & \delta\tilde{\phi}_{\text{rms}} &\equiv \sqrt{\frac{1}{N} \sum_p (\delta\tilde{\phi}_p)^2}, \\ \delta\tilde{a}_{\text{avg}} &\equiv \frac{1}{N} \sum_p \delta\tilde{a}_p, & \delta\tilde{a}_{\text{rms}} &\equiv \sqrt{\frac{1}{N} \sum_p (\delta\tilde{a}_p)^2}, \end{aligned} \quad (13)$$

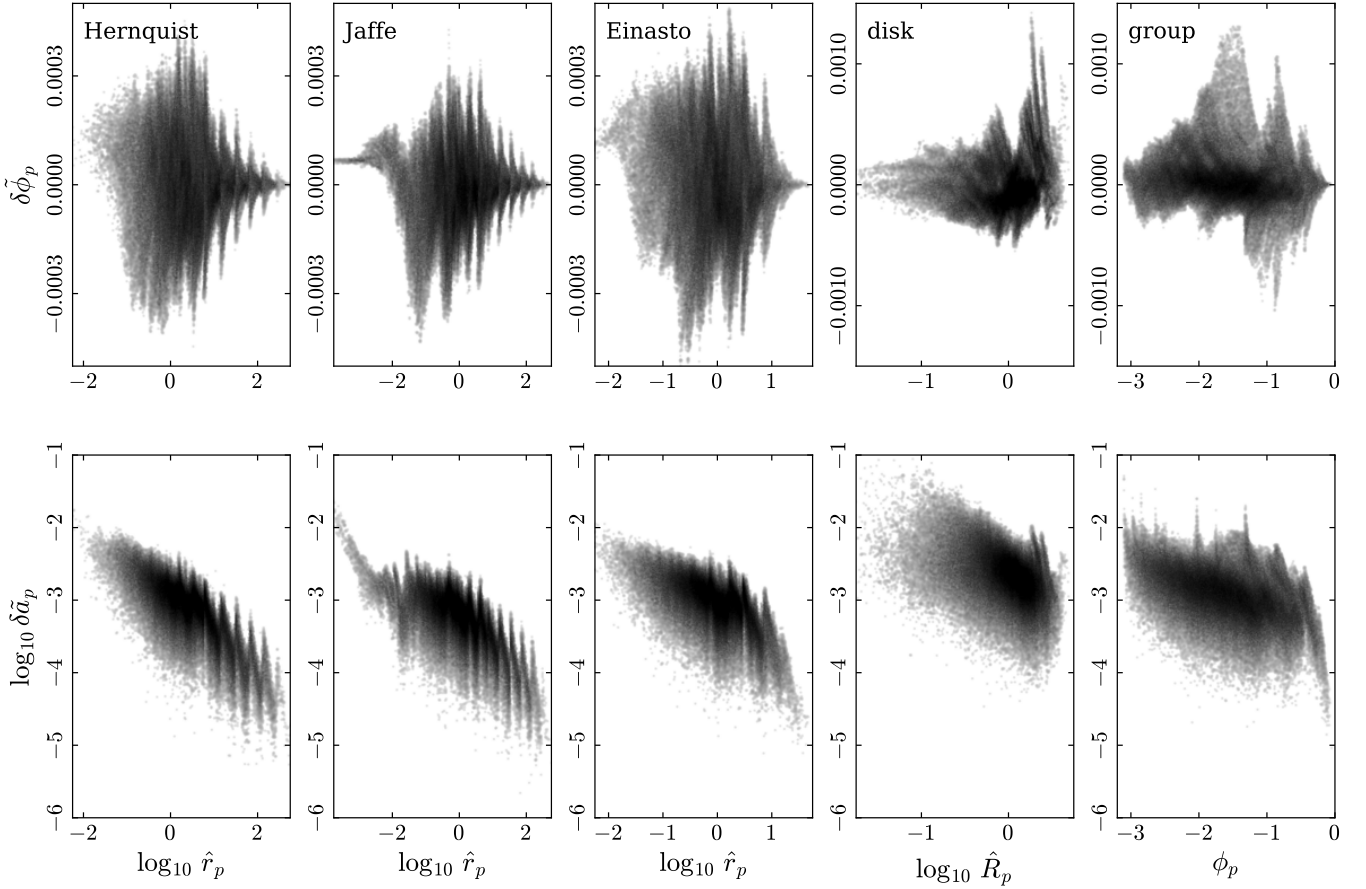


Figure 4. Particle-by-particle errors versus distance from centre or potential. The top row plots relative potential error, while the lower one plots log relative acceleration error. Forces were calculated using opening angle $\theta = 0.8$; quadrupole terms were corrected for softening, with $\epsilon = 0.01$. Each realization has $N = 2^{18}$ bodies.

Fig. 6 shows how these errors depend on opening angle θ for all five mass models. The five realizations of each model are plotted separately; each has $N = 2^{18}$ particles.

The upper left panel of this figure shows the relationship between θ and the mean relative potential error $\delta\tilde{\phi}_{\text{avg}}$, which measures the net bias away from $\delta\tilde{\phi} = 0$ in Fig. 5. Since this bias may have either sign, the vertical axis uses a linear scale. It's evident that biases decrease as $\theta \rightarrow 0$, but the manner of convergence depends on the mass model. The three spherical models seem to be slightly biased toward $\delta\tilde{\phi}_{\text{avg}} < 0$ for $\theta \geq 0.7$ but converge rapidly as θ decreases. On the other hand, the group models, each composed of four spherical components with random positions, are biased toward $\delta\tilde{\phi}_{\text{avg}} > 0$ and converge more slowly. Finally, the disc models, with random positions and orientations, exhibit dramatic variations from one realization to the next; these models appear to be biased toward $\delta\tilde{\phi}_{\text{avg}} > 0$ for $\theta > 0.8$, but the other way for $\theta < 0.8$.

The upper right panel of Fig. 6 plots RMS relative potential errors $\delta\tilde{\phi}_{\text{rms}}$, which effectively measure the spread around $\delta\tilde{\phi} = 0$. Since the spread is positive-definite, logarithmic scaling can be used on the vertical axis. In general, the RMS errors are rather similar for all five models, although the disc and group models yield larger errors for a given θ , and exhibit larger variations within their respective ensembles. This plot shows that $\delta\tilde{\phi}_{\text{rms}}$ follows rough power-law relationships with θ . The color-coded lines give the slopes; all five models are fairly well fit by $\delta\tilde{\phi}_{\text{rms}} \propto \theta^{(3.3 \pm 0.3)}$.

The two bottom panels plot average (left) and RMS (right) relative acceleration errors. These plots are quite similar, implying that the error distributions are not dominated by outliers. Consistent with previous results, disc and group models produce the largest acceleration errors, although variations among members of the disc and group ensembles are smaller than those seen for potential errors. Acceleration errors fall rapidly as θ is reduced. Power-law fits yield $\delta\tilde{a}_{\text{rms}} \propto \theta^{3.4 \pm 0.2}$ for the three spherical models; the disc models converge even faster, with $\delta\tilde{a}_{\text{rms}} \propto \theta^{4.0}$.

For completeness, Supplemental Fig. 1 shows how errors vary with θ when forces are computed *without* quadrupole terms. In general, there's little reason not to use quadrupole terms (Hernquist 1987); the saving in computing time is relatively modest, while the additional errors incurred are quite large. The disc model in particular is handled very poorly without quadrupole terms, because a good part of the long-range force is due to cells which sample substantial pieces of the disc; these cells will have large quadrupole moments which are neglected in Supplemental Fig. 1. For the Hernquist and Einasto models, acceleration errors scale roughly as $\delta\tilde{a}_{\text{rms}} \propto \theta^{2.4 \pm 0.3}$; the Jaffe model converges a bit more slowly.

By way of comparison, Makino (1990b) derived large- N scaling laws of the form $\delta\tilde{a}_{\text{rms}} \propto \theta^{7/2}$ (with quadrupole moments) or $\delta\tilde{a}_{\text{rms}} \propto \theta^{5/2}$ (without). This calculation assumed a homogeneous particle distribution, implying that the quadrupole and octupole moments of cells are due entirely to Poissonian fluctuations (Barnes

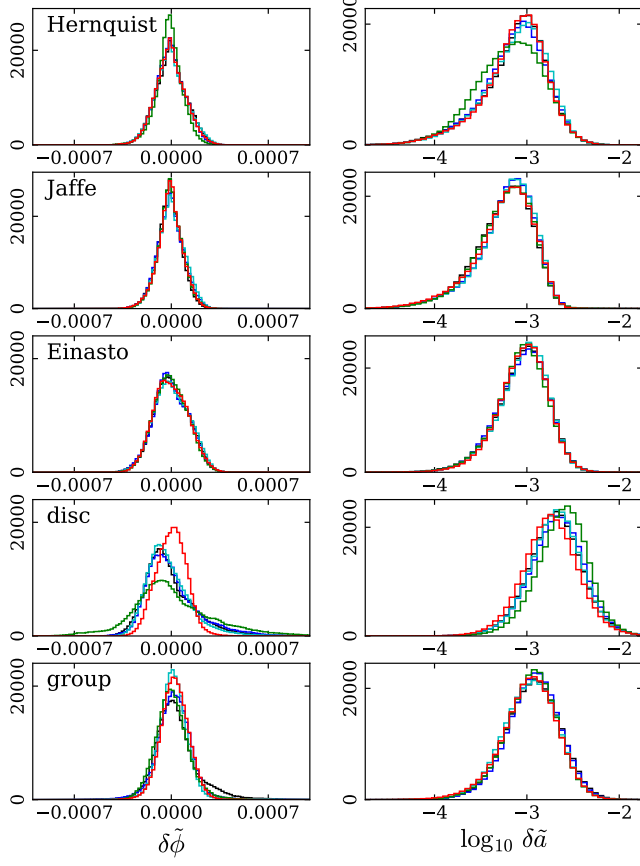


Figure 5. Distributions of relative potential errors (left) and log relative acceleration errors (right) for all five models. Forces were calculated as in Fig. 4. A different color is used for each realization.

& Hut 1989), and that separate cells are statistically independent. The power laws reported above are broadly consistent with Makino’s predictions. However, this agreement may be partly fortuitous; trees constructed for inhomogeneous models contain cells which sample gradients or large-scale features in the mass distribution, and these cells have octopole-plus moments which are not necessarily dominated by Poissonian noise.

Potential and acceleration errors gradually decrease as N increases (Hernquist 1987). Supplemental Fig. 2 illustrates the relationship between N and $\delta\tilde{a}_{\text{rms}}$, computed using opening angle $\theta = 0.8$. For the values of N used here, acceleration errors follow rough power-laws, $\delta\tilde{a}_{\text{rms}} \propto N^\beta$, with indices in the range $\beta \simeq -0.07$ to -0.15 (summarizing for $\theta \in [0.4, 0.8]$). As N grows, the cells contributing to the field of a typical particle are increasingly well-populated; this should reduce the stochastic part of their octopole-plus moments (Barnes & Hut 1989) and therefore drive down the overall error. If this explanation is correct, force errors should level off in the $N \rightarrow \infty$ limit.

3.4.1 Softening corrections

Fig. 7 shows how the quadrupole softening correction (eq. 6) improves force calculations. For the softening length $\epsilon = 0.01$ adopted here, the Jaffe model (red) is the only one which exhibits a large effect. This model contains a non-trivial amounts of mass (~ 1 per cent) within a radius $r = \epsilon$ of its centre. The correction dramatically

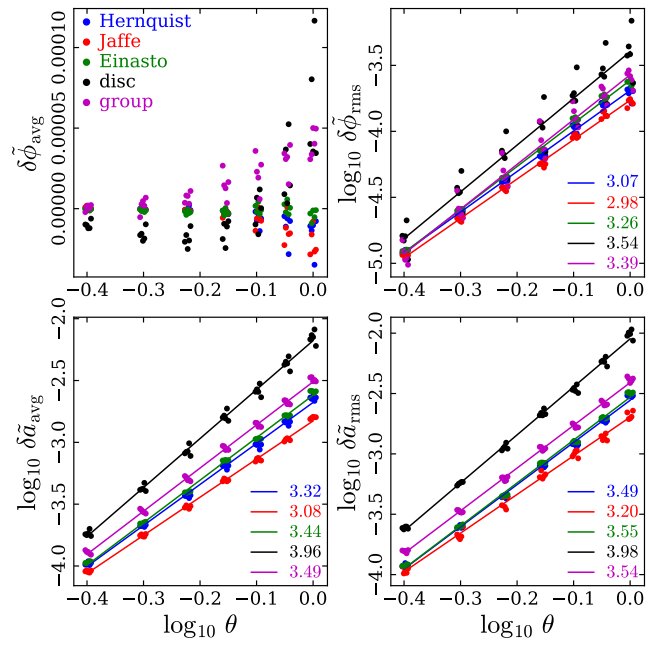


Figure 6. Mean and RMS errors versus log opening angle. Top row shows potential errors, bottom shows acceleration; left column shows means, right shows RMS. Forces were calculated as in Fig. 4. Each model is represented by five realizations of $N = 2^{18}$ bodies; $\log_{10} \theta$ values are plotted with small offsets to reduce crowding. The upper-left panel uses a linear y-axis since $\delta\tilde{\phi}_{\text{avg}}$ may have either sign. The other three panels employ log-log scaling; thin lines are least-squares fits, with the slopes listed in the lower right.

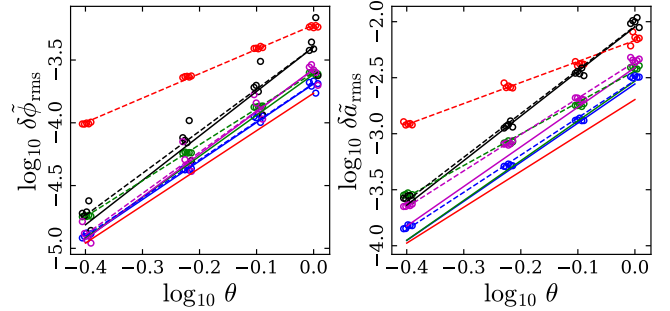


Figure 7. RMS potential (left) and acceleration (right) errors vs. opening angle. Open markers and dashed lines were computed without the softening correction to the quadrupole term, while solid lines, copied from Fig. 6, include this correction.

improves the accuracy of the calculations; for $\theta = 1$, the corrected potential and acceleration are ~ 3 times more accurate, while for $\theta = 0.4$, they are a factor of ~ 10 better. Without the correction, the distributions of $\delta\tilde{\phi}$ and $\delta\tilde{a}$ have tails *much* larger than typical errors. These arise from particles within a radius $\hat{r} \sim 10\epsilon$ from the centre (Barnes 2012, Appendix B), and account for the dramatic effects seen here.

Results for the other mass models also improve, albeit some by only a few per cent. The correction yields essentially *no* benefit for Hernquist and disc models. In these models, cells within distances of a few ϵ contribute relatively little to the gravitational field; consequently, the net effect of the errors associated with these cells is

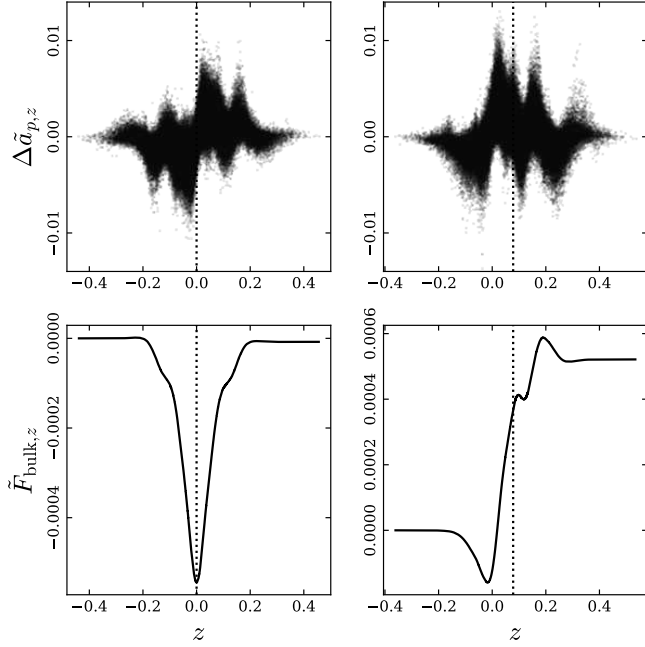


Figure 8. Origin of bulk forces on a disc system. Top panels are scatter-plots of z -component acceleration errors vs. z ; bottom panels show z -component of bulk force for all particles with positions $< z$. Dotted line shows the position of the disc's midplane.

small. Of course, this depends on the softening length; a rough generalization is that softening corrections are likely to be important if a few per cent of the total mass lies within a sphere of radius ϵ – as is the case for the Jaffe model.

3.5 Bulk Forces

Newton's third law implies that the total force on an isolated system always vanishes: $\mathbf{F}_{\text{bulk}} = \sum m_p \mathbf{a}_p = 0$. As Fig. 1 demonstrates, forces computed using a tree-code don't obey this law. The bulk force generated by a tree-code is the sum of the force errors for individual particles:

$$\tilde{\mathbf{F}}_{\text{bulk}} \equiv \sum_p m_p \tilde{\mathbf{a}}_p = \sum_p m_p \Delta \tilde{\mathbf{a}}_p. \quad (14)$$

If the errors $\Delta \tilde{\mathbf{a}}_p$ were statistically independent, the second sum in eq. 14 could be treated as a random walk. The magnitude of the bulk force could then be estimated as $\tilde{F}_{\text{bulk}} \simeq \Delta \tilde{F}_{\text{rms}} \sqrt{N}$, where $\Delta \tilde{F}_{\text{rms}}$ is the RMS force error. However, § 3.2 has already presented a situation in which the force errors on adjacent particles are clearly correlated. As a result, bulk forces are generally much larger than a random-walk model would predict.

Fig. 8 examines the origin of the bulk force on the disc in Fig. 1. The left-hand panels of this figure show results for a disc centred on the origin, while the right-hand panels show what happens when the disc is offset by $\Delta z = 5/64$, which yields a large bulk force. Top panels show accelerations, plotting the z -component of each particle's error against its z position. The complex structure visible in these scatter-plots confirms that adjacent particles have correlated errors. If the disc is symmetrically placed with respect to the tree, as on the left, the error distribution is also symmetric; particles below (above) the disc's midplane feel spurious downward (upward) forces.

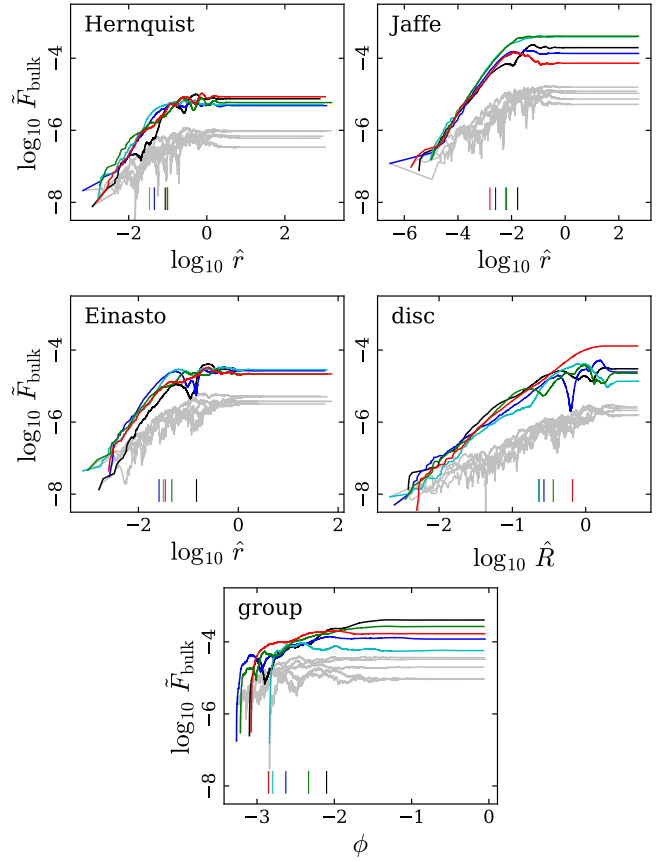


Figure 9. Accumulation of bulk forces in all five mass models. Forces in each panel are summed by the variable used for the horizontal axis; colored curves are actual results, while light grey curves show random walks with the same stepsizes. All realizations have $N = 2^{18}$ particles; forces are calculated with $\theta = 0.8$. Short vertical marks at the bottom of each panel show where the bulk force reaches half of its final value.

Conversely, if the disc is displaced, as on right, the distribution is still correlated, but no longer symmetric.

The bottom panels of Fig. 8 show how the bulk forces accumulate if the second sum in eq. (14) is ordered by the z -coordinate of each particle. On the left, the errors due to particles below the midplane are almost perfectly canceled by those above. As a result, the bulk force is very small; it would vanish entirely if not for low-level asymmetries due to sampling the density field with a finite number of particles. This error cancellation is spoiled if the disc is shifted along the z axis; as the right-hand panel shows, the result is a substantial bulk force in the positive z direction.

Although the disc model provides perhaps the clearest example of bulk forces, it is not unique. Fig. 9 shows how individual force errors accumulate to yield bulk forces for all five mass models. In each panel, the sum in eq. (14) is ordered by the quantity shown on the horizontal axis: distance \hat{r} from the model centre for the three spherical models, cylindrical radius \hat{R} for the disc models, and direct-sum potential ϕ for the group models. The five colored curves show actual bulk forces, while the light grey curves were generated by replacing each $\Delta \tilde{\mathbf{a}}_p$ in eq. (14) by a randomly-oriented vector of the same magnitude. Thus, the grey curves show how bulk forces would accumulate if force errors were uncorrelated. In every case, the actual bulk forces are roughly an order of magnitude greater than their uncorrelated counterparts, demonstrating the ubiquity of error

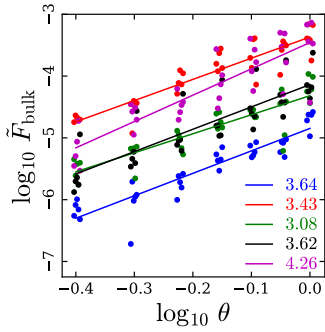


Figure 10. Bulk forces vs. opening angle. Mass models are realized with $N = 2^{18}$ particles. Individual realizations are plotted as dots, color-coded as in Fig. 6; solid lines are least-square fits with slopes as shown.

correlations and their consequences for violations of Newton’s third law.

Fig. 9 illustrates a few other points as well. In each panel, short vertical marks indicate the radius (or potential) where the bulk force reaches half its final value. For the three spherical models, these radii are up to two orders of magnitude *smaller* than their respective half-mass radii; thus, bulk forces are dominated by a minority of particles with larger-than-average force errors (see Fig. 4). In effect, these fictitious forces tug the centres of systems around, dragging the rest in due course. It is also striking that the bulk forces on Jaffe model are ~ 30 times larger than on Hernquist models, even though both have similar relative acceleration errors. Moreover, while all five members of the Hernquist and Einasto ensembles have similar bulk forces, the Jaffe ensemble displays a much larger range; evidently these bulk force are quite sensitive to the placement of the central $\rho \propto r^{-2}$ cusp relative to the tree.

The disc models also exhibit large variations within their ensemble. This is not surprising; Fig. 8 already shows how the bulk force on a disc depends on its position. In addition, bulk forces on discs are sensitive to orientation. The disc shown in red provides a striking example; as Fig. 5 shows, this disc yields *better* accelerations than other the members of its ensemble do, yet here it generates a bulk force nearly an order of magnitude *larger*! This occurs because the close alignment of this disc with the x - z plane produces acceleration errors which add coherently. In contrast, the other four disc realizations all have larger misalignments; in every case, their acceleration errors are larger, but these errors are less coherent, resulting in smaller bulk forces. Moreover, these forces are not necessarily perpendicular to the disc plane; indeed, the disc shown in cyan, which has the largest acceleration errors, generates a bulk force nearly parallel to the disc.

Unlike the other four examples, the group models are not spherically or rotationally symmetric. This virtually guarantees that they will generate large bulk forces, since symmetric error patterns like that seen in the top-left panel of Fig. 8, which tend to self-cancel, almost never occur. It’s noteworthy that these forces are substantially larger than those obtained for the Einasto models making up these groups. The median potential for this ensemble is $\phi_{\text{med}} \approx -1.63$; just as in the spherical models, a minority of particles, lying deep within the potential well, account for most of the bulk forces. Finally, the heterogeneous nature of the group models also ensures that there are significant variations between realizations.

Fig. 10 plots bulk forces vs. opening angle for various mass models. This plot indicates that the results above, obtained with $\theta = 0.8$, generalize to other opening angles as well. For the four intrinsically symmetric models, bulk forces scale as $\tilde{F}_{\text{bulk}} \propto \theta^{3.4 \pm 0.2}$, similar to the scaling of $\delta\tilde{a}_{\text{rms}}$ seen in § 3.4. This may indicate that the level

of error correlation is not very sensitive to the value of θ . On the other hand, the group models converge like $\tilde{F}_{\text{bulk}} \propto \theta^{4.3}$, which is somewhat faster than the slope of ~ 3.5 they yield for $\delta\tilde{a}_{\text{rms}}$.

3.6 Bulk Torques

Newtonian mechanics tells us that the total torque on an isolated system vanishes: $\mathbf{T}_{\text{bulk}} = \sum m_p \mathbf{r}_p \times \mathbf{a}_p = 0$. The third law is necessary but not sufficient for this to be true; besides being equal and opposite, forces must point in the right *directions*. For example, consider a binary system consisting of two spherical, well-separated galaxies. The net forces on the two galaxies may be equal and opposite, but if they are not accelerating *directly* toward each other, the bulk torque on the system will not vanish. Thus, particle-mesh and tree algorithms which enforce Newton’s third law can still violate angular momentum conservation (Hernquist 1987; Marcello 2017; Korobkin et al. 2021).

In the presence of bulk forces, some care is needed to define bulk torques. Imagine a system, whose centre-of-mass is offset from the origin of the simulation CS by \mathbf{r}_{cm} , subject to a treecode-induced bulk force $\tilde{\mathbf{F}}_{\text{bulk}}$. The cross-product of these two vectors has the characteristics of a torque, but it does not tell us anything about the rate at which the system’s *internal* angular momentum changes. For that, we need to look at the bulk torque calculated in the system’s centre-of-mass frame:

$$\tilde{\mathbf{T}}_{\text{bulk}} \equiv \sum_p m_p (\mathbf{r}_p - \mathbf{r}_{\text{cm}}) \times \tilde{\mathbf{a}}_p = \sum_p m_p \bar{\mathbf{r}}_p \times \Delta \tilde{\mathbf{a}}_p, \quad (15)$$

where $\bar{\mathbf{r}}_p$ is the position relative to the centre of mass.

Once again, discs provide an intuitive way to see how bulk torques can arise. As Fig. 8 shows, a disc which lies in the x - y plane but is slightly offset in the z direction feels a bulk force pushing it further away from the origin. Consider now a disc which is not offset but rather slightly tilted; the side above the x - y plane feels an upward force, while the side below feels a downward force. In other words, the disc feels a torque which acts to increase its initial tilt.

Fig. 11 shows how errors accumulate to yield bulk torques for all five models. These torques are evaluated in each realization’s centre-of-mass coordinate system. The conventions used in this plot are the same used in Fig. 9; in particular, colored curves represent actual torques for each realization, while light grey curves show random-walk equivalents.

All three spherical models yield bulk torques of fairly similar magnitude. The Jaffe model is somewhat of an outlier, with median torques ~ 5 times larger than the other two, and a somewhat larger scatter between realizations. In most cases, bulk torques arise at larger radii than bulk forces, presumably because larger radii provide longer lever arms. Finally, actual torques, especially for the Hernquist and Einasto models, are typically only a few times larger than those expected in the absence of correlations. Torques on spherical models presumably arise from Monte-Carlo sampling of their mass distributions. If so, they should scale with particle number as $T_{\text{bulk}} \propto N^{-1/2}$. Actual torques for the three spherical models are roughly consistent with this prediction; fitting $\log T_{\text{bulk}}$ to $\log N$ yields power-law indices of -0.56 , -0.68 , and -0.46 for the Hernquist, Jaffe, and Einasto models, respectively, with no systematic dependence on θ .

The disc models experience substantially larger bulk torques than any of the spherical models do. As the discussion above implies, orientations appear to be the main source of the rather sizable variation among disc realizations, although offsets also contribute. Actual torques are an order of magnitude larger than uncorrelated errors predict, with much of this difference arising at scales larger than

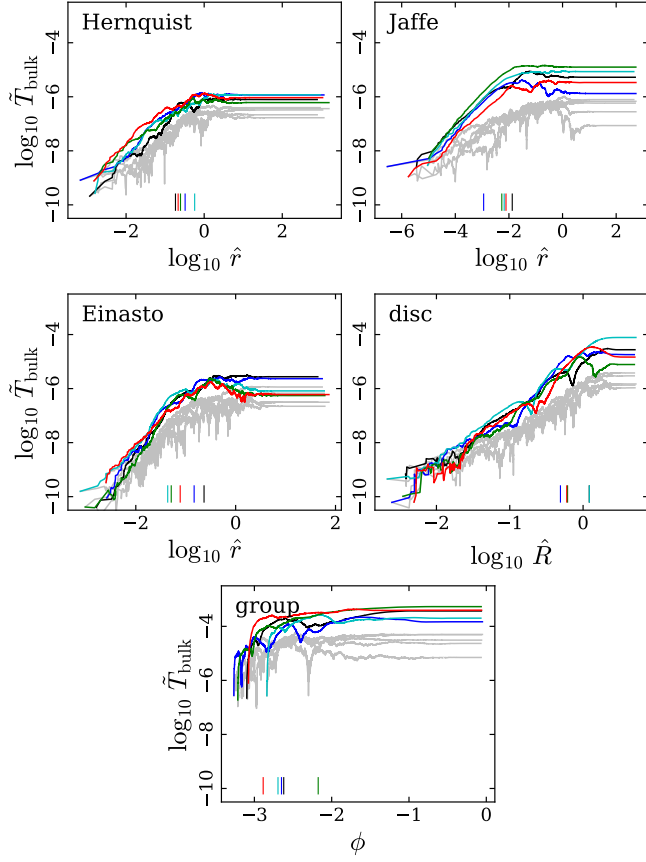


Figure 11. Accumulation of bulk torques in all five mass models. Compare with Fig. 9, which also describes plotting conventions.

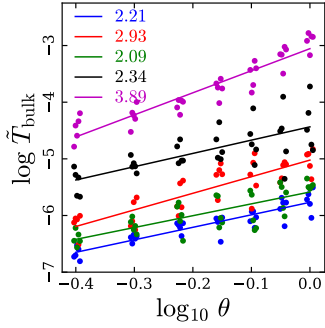


Figure 12. Bulk torques vs. opening angle. Compare with Fig. 10.

$\log_{10} \hat{R} > -1$, which is approximately the disc's scale-height. Bulk torques on discs appear to be independent of N , which makes sense since irregularities due to Monte-Carlo are not necessary.

By virtue, again, of their *intrinsic* asymmetries, the group models yield the largest bulk torques. Correlations play a significant role in generating these torques. Half of the total torque is exerted on particles deep within the multiple potential wells of these groups. Again, these torques show no systematic dependence on particle number.

Fig. 12 plots bulk torques against opening angle. Torques on the spherical models are numerically small, but decline fairly slowly, roughly as $T_{\text{bulk}} \propto \theta^{2.0 \pm 0.1}$. Disc torques are larger and follow a

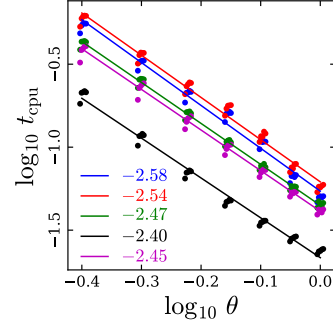


Figure 13. Computing time in minutes vs. opening angle θ for models color-coded as in Fig. 6. Each configuration has $N = 2^{18}$ particles. Quadrupole terms are included. The thin lines are least-squares fits, with slopes shown in the lower left.

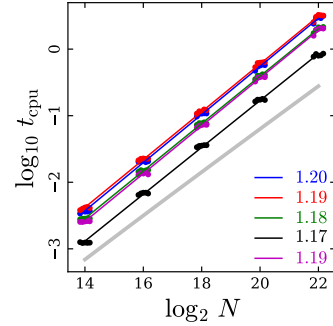


Figure 14. Computing time in minutes vs. number of particles for different models. Forces were calculated as in Fig. 4. These timings are for $\theta = 0.8$ and include quadrupole terms. Thin lines are least-squares fits, with slopes for each shown in the lower right. Plotted $\log N$ values are randomly offset by small amounts to reduce crowding. The light grey curve shows a $N \log(N)$ relationship.

similar trend with opening angle. On the other hand, the torques on the group models decline more rapidly, roughly as $\theta^{4.0}$.

3.7 Computing Time

Fig. 13 shows how computing time⁵ depends on the opening angle. All five models yield rough power-law relationships approximating $t_{\text{cpu}} \propto \theta^{-2.5}$. CPU time for a given θ is model-dependent; the disc takes roughly a third of the time required by the Hernquist and Jaffe models. The latter are slower, in part because – even with a taper at radius $b = 100$ – they include a few bodies with very large radii. To accommodate these outliers, a large root cell is required, and it must be subdivided quite deeply to fully resolve the body distribution. This makes tree descent more costly.

The power-laws in Figs. 6 and 13 can be combined to obtain a relationship between computing time and accuracy. For example, eliminating θ from $\delta a_{\text{rms}} \propto \theta^{3.5}$ and $t_{\text{cpu}} \propto \theta^{-2.5}$ yields $\delta a_{\text{rms}} \propto t_{\text{cpu}}^{-1.4}$. This is confirmed by plotting δa_{rms} against t_{cpu} (see Supplemental Fig. 3). Remarkably, much of the model-to-model variation in Figs. 6 and 13 cancels out, leaving a near-universal relationship between computing time and accuracy.

Finally, Fig. 14 examines the relationship between computing time

⁵ CPU times were measured using an Intel i7 processor with a baseline clock rate of 3.40 GHz.

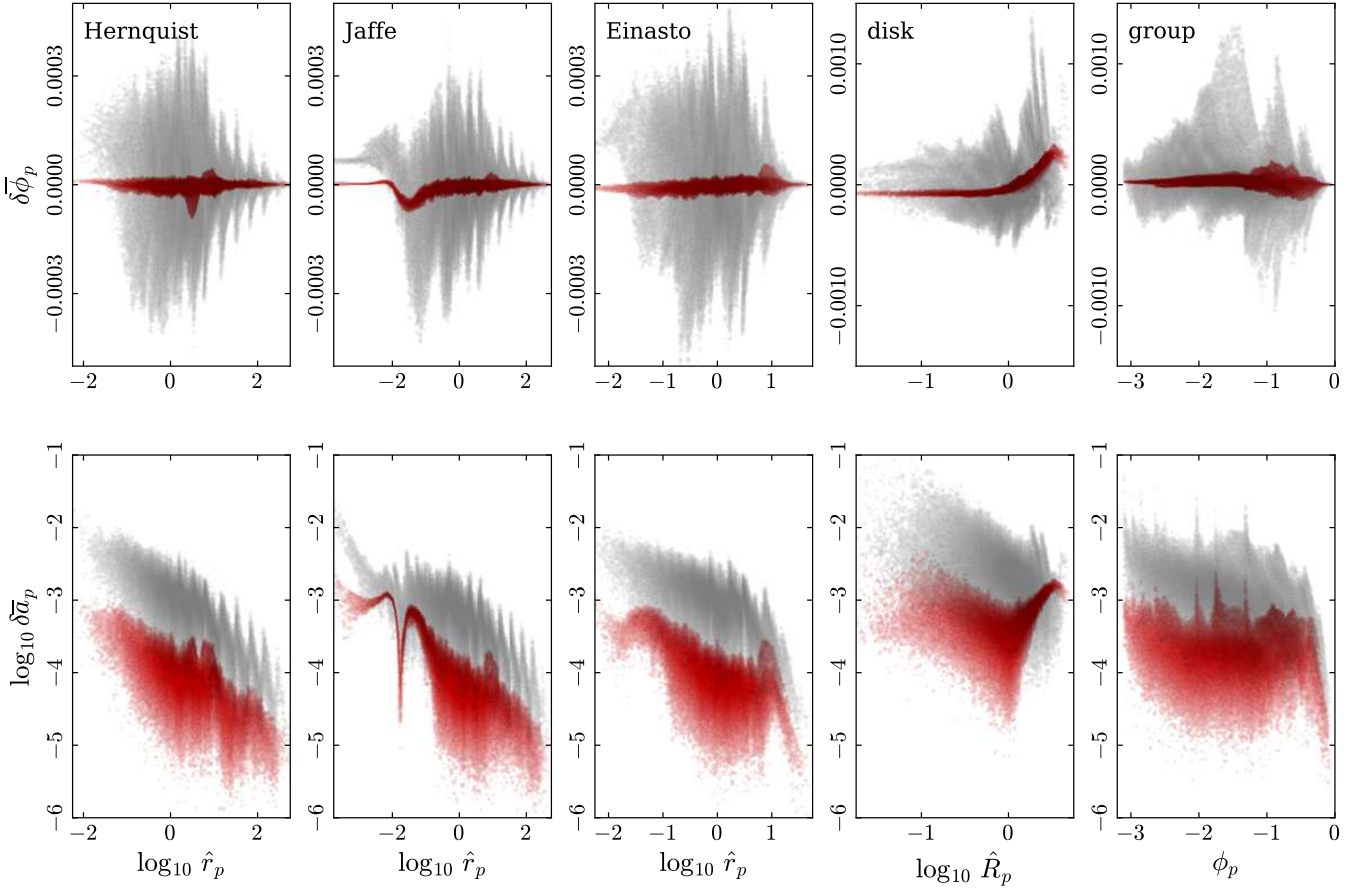


Figure 15. Scatter-plots of force calculation errors versus radius or potential. Layout follows Fig. 4. Results of averaging over $N_{\text{avg}} = 256$ trees are shown in red, while non-averaged results are shown in grey.

and number of particles for $\log_2 N = 14, 16, \dots, 22$. Over this range of N , all five models follow power laws with slopes which are weakly dependent on θ ; for $\theta = 1.0$ the slope is 1.13 ± 0.02 (one-sigma), while for $\theta = 0.4$ it is 1.25 ± 0.03 . It makes sense that the slope increases as θ decreases; in the limit $\theta \rightarrow 0$, the tree-code behaves like a direct-sum code, implying a slope of 2. In the figure, a light grey curve shows a $t_{\text{cpu}} \propto N \log(N)$ relationship; this curve has an average slope of 1.08. Thus, for the values of N tested here, the computing time grows *slightly* faster than $N \log(N)$.

4 TREE AVERAGING

As § 3 shows, the forces returned by a single hierarchical calculation include errors which are peculiar to the specific tree CS employed. These errors will partly cancel if results from multiple, independent trees are averaged together. Let $(\mathbf{R}_k, S_k, \mathbf{T}_k)$, where $k = 1, \dots, N_{\text{avg}}$, be a series of tree CSs chosen at random. Let $\tilde{\phi}_{p,k}$ and $\tilde{\mathbf{a}}_{p,k}$ be the potential and acceleration of particle p computed using tree CS k . Then the ‘tree-averaged’ potential and acceleration of p are

$$\bar{\phi}_p = \frac{1}{N_{\text{avg}}} \sum_{k=1}^{N_{\text{avg}}} \tilde{\phi}_{p,k}, \quad \bar{\mathbf{a}}_p = \frac{1}{N_{\text{avg}}} \sum_{k=1}^{N_{\text{avg}}} \tilde{\mathbf{a}}_{p,k}. \quad (16)$$

As the number of independent tree CSs grows, these averages should better approximate the true potential ϕ_p and acceleration \mathbf{a}_p .

Fig. 15 shows that averaging can significantly reduce tree-code errors. Here the red points show the results of averaging over $N_{\text{avg}} = 256$ trees, each employing a different rotation, scaling, and translation⁶. The black points, copied directly from Fig. 4, are not averaged. In every case, the averaged potentials are much more accurate than their counterparts. Likewise, the acceleration errors, plotted on a logarithmic scale, are about an order of magnitude smaller. Averaging has largely erased the oct-tree signatures exhibited by the black points. For the spherical models, the regular bars seen in the $\delta\tilde{\phi}_p$ distributions have vanished, and the sawtooth patterns in the $\delta\tilde{a}_p$ distributions are smoothed out. The offset in the Jaffe model’s central potential, noted in § 3.3, has vanished as a result of averaging over position. For the disc and group models, the chaotic patterns in $\delta\tilde{\phi}_p$ are largely suppressed.

All the same, averaging over tree CSs has not *entirely* eliminated errors in potential and acceleration. The Jaffe model provides a clear example, with conspicuous features visible in both the $\delta\tilde{\phi}_p$ and $\delta\tilde{a}_p$ distributions near $\log_{10} \hat{r}_p \simeq -1.7$. The same pattern of acceleration errors appears to be replicated in the Hernquist and Einasto models, although less prominently as these models are sparsely populated

⁶ For these tests, I set the maximum translation distance $T_{\text{max}} = 4$ length units – the distance between adjacent sweet spots for the Hernquist models (§ 3.3). This does not seem to be a critical choice; virtually identical results are obtained for all models with $T_{\text{max}} = 1$.

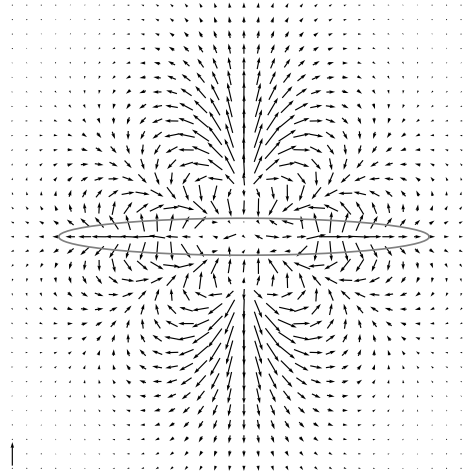


Figure 16. Residual acceleration errors for a Gaussian disc, viewed edge-on. Forces computed with $\theta = 0.8$ were averaged over $N_{\text{avg}} = 256$ CSs. The oval curve, which represents the disc, extends ± 4 and ± 0.4 length units along the x and z axes, respectively. For scale, the vertical arrow at the lower left shows an acceleration error $|\Delta\bar{\mathbf{a}}| = 0.0003$.

at such small radii. Briefly, the inward acceleration is *slightly* over-estimated, by at most ~ 0.08 per cent (assuming $\theta = 0.8$), for radii $\log_{10} \hat{r} \gtrsim -1.7$, and under-estimated, by a comparable amount, at smaller radii. The radial scale of these features is comparable to the softening length $\epsilon = 0.01$, suggesting a link to residual errors in the softened quadrupole term (eq. 6).

The disc model offers another kind of example, with positive $\delta\bar{\phi}_p$ within $\log_{10} \hat{R}_p \lesssim 0$, and negative elsewhere. This is *not* related to softening; rather, the sign-change occurs near the half-mass radius ($\log_{10} \hat{R}_{\text{half}} \simeq 0.07$). A connection to the physical scale of the model is bolstered by the acceleration errors (lower panel), which are suppressed by roughly an order of magnitude for $\log_{10} \hat{R}_p \lesssim 0$, but approach the non-averaged errors at larger radii.

Residual acceleration errors $\Delta\bar{\mathbf{a}} = \bar{\mathbf{a}} - \mathbf{a}$ generated by the disc model are mapped in Fig. 16. The global pattern seen here is independent of θ ; only the amplitude changes. It is likewise invariant with respect to rotation about the z -axis and reflection across the xy -plane. The octapole component dominates, with significant higher-order contributions. Small irregularities (e.g., within the central few grid-points) arise from (1) sampling the density field with $N = 2^{18}$ particles, and (2) averaging over $N_{\text{avg}} = 256$ tree CSs; tests with different CS sequences and different realizations indicate that sampling effects dominate the irregularities.

In Fig. 16, one can easily find closed paths around which line integrals are non-zero; thus $\Delta\bar{\mathbf{a}}$ is not the gradient of any function. Since the true acceleration is the gradient $\mathbf{a} = \nabla\phi_\epsilon$, where ϕ_ϵ is the softened N-body potential, it follows that $\bar{\mathbf{a}}$ is not a perfectly conservative force field.

These error patterns become evident for any reasonably large value of N_{avg} . They arise because oct-tree gravity calculations make *systematic* errors which are not tied to the choice of coordinate system. Rather, such errors are generic to the whole *approximation scheme*. A particle at the outskirts of a thin disc interacts with many cells which enclose substantial chunks of the disc, and therefore have large octapole-plus moments. This is true regardless of the CS used to construct the tree, so its consequences will be manifest even after averaging over multiple CSs.

To see how errors in the averaged potential and acceleration depend

on the number of averages, I define aggregated RMS errors $\delta\bar{\phi}_{\text{rms}}$ and $\delta\bar{a}_{\text{rms}}$ by analogy with eq. (13). Fig. 17 presents log-log plots of these errors versus N_{avg} . A different seed was used to generate the set of random transformations $(\mathbf{R}_k, \mathbf{S}_k, \mathbf{T}_k)$ for each realization and choice of N_{avg} . Thus, while the same five realizations were tested for multiple values of N_{avg} , the transformations used are independent. In each panel, thin lines show individual realizations, a heavy black line shows the median relationship between N_{avg} and $\delta\bar{\phi}_{\text{rms}}$ or $\delta\bar{a}_{\text{rms}}$ obtained using rotation, translation, and scaling together, while a grey dotted line shows a power-law $\propto N_{\text{avg}}^{-1/2}$. This is the relationship the central limit theorem would predict in the absence of systematic errors.

For modest values of N_{avg} , the averaged potential and acceleration errors for the spherical models do in fact scale roughly as $N_{\text{avg}}^{-1/2}$. However, as N_{avg} grows, the errors ‘peel away’ from this ideal trend and seem to be leveling off. As a conceptual model, the error for a given particle may be split into two parts: a *random* part which depends on the tree CS, and a *systematic* part which is independent of the tree CS. Averaging suppresses the random part by a factor of $N_{\text{avg}}^{-1/2}$, but has no effect on the systematic part. In the Hernquist and Einasto models, random errors are much larger than systematic ones, so averaging provides significant improvements before the systematic errors dominate. Systematic acceleration errors appear larger for the Jaffe models; as a result, the $\delta\bar{a}_{\text{rms}}$ curves deviate from $N_{\text{avg}}^{-1/2}$ earlier.

If systematic errors are comparable to random ones then tree averaging will provide limited benefits. This is presumably the case for the disc and group potentials: median errors decrease by factors of ~ 2 and ~ 2.5 respectively as N_{avg} increases, compared to the order-of-magnitude reductions the spherical models enjoy. Moreover, the group models exhibit especially large variations between realizations, implying that the layout of the mass distribution strongly influences the level of systematic error. However, the corresponding acceleration errors (bottom panel) exhibit better convergence; this is encouraging as accurate accelerations are more critical for simulations than accurate potentials.

The results described so far employ all three tree transformations: rotation, scaling, and translation. How do these transformations contribute individually? The red, green, and blue curves in Fig. 17 address this question by plotting $\delta\bar{\phi}_{\text{rms}}$ and $\delta\bar{a}_{\text{rms}}$ as functions of N_{avg} for each transformation separately. For the spherical models, the upshot is that rotation (green) is by far the most effective, accounting in each case for a large part of the overall improvement, while translation (red) and scaling (blue) provide smaller and roughly comparable benefits. One of the Einasto realizations benefits less from rotation than do the other four; it has a smaller offset ($r_{\text{off}} \simeq 1.23$, compared to a mean of 3.18 for the rest), so random rotations don’t displace its centre as much. Clearly, rotation alone will confer little benefit for spherical models situated near the origin.

A different pattern emerges for the disc models. Rotation and translation appear to be equally effective, and each in isolation is almost as good as all three transformations together. By itself, scaling offers somewhat greater benefits than it does for the spherical models, with noticeable variations in acceleration errors among the five realizations.

For the group models, rotation again provides the largest gain in accuracy, especially for accelerations. However, this benefit varies significantly from one realization to the next. In contrast, translation and scaling yield modest improvements, of comparable magnitude, with less variation among realizations.

Do the advantages of averaging persist for other choices of opening angle? Fig. 18 shows how RMS errors in averaged potential and

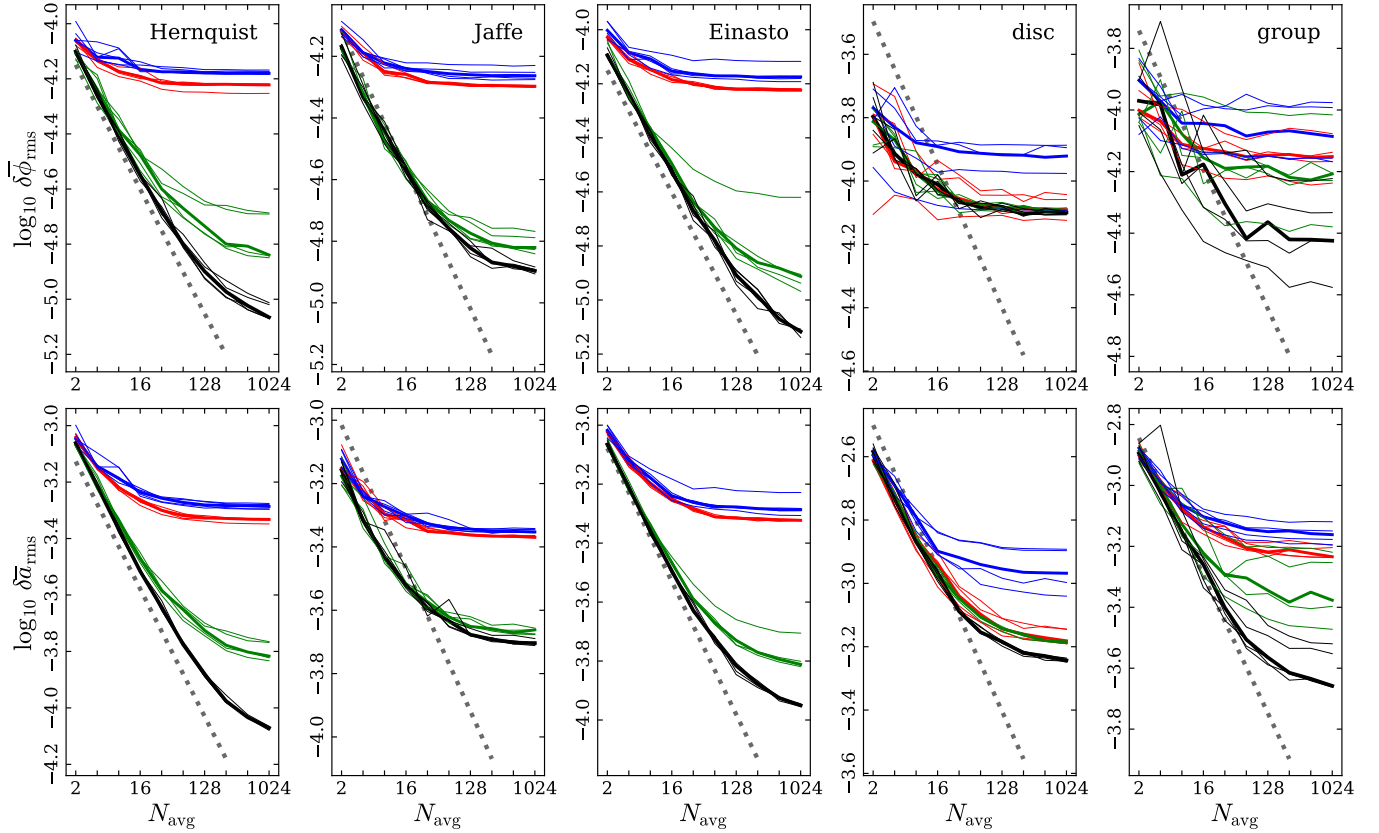


Figure 17. RMS errors in tree-averaged potentials (top) and accelerations (bottom) vs. number of averages, using $N = 2^{18}$ particles and $\theta = 0.8$. In each panel, black curves show results for all three transformations together; red, green, and blue curves show results for translation, rotation, and scaling, respectively; a grey dotted line shows the scaling $\propto N_{\text{avg}}^{-1/2}$ expected from the central limit theorem. Thin lines represent individual realizations, while heavier lines show medians.

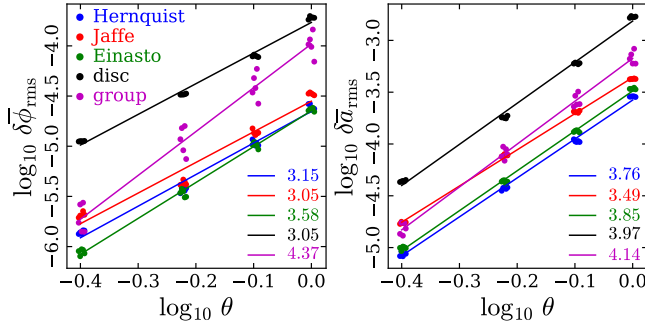


Figure 18. Tree-averaged RMS errors versus log opening angle. $N_{\text{avg}} = 256$ averages were used for each calculation. Compare with right panels of Fig. 6.

acceleration depend on θ . Comparison with Fig. 6 confirms that averaging and opening angle work well together; errors averaged over $N_{\text{avg}} = 256$ trees decrease as least as fast as un-averaged errors as θ is reduced. Forces for Hernquist and Einasto models become a factor of ~ 10 more accurate; the other models improve by factors of ~ 6 or more.

Fig. 19 show how bulk forces and torques behave as the number of random tree CSs increases. Since bulk forces and torques are residuals left after near-cancellation between N approximate accelerations, the results tend to be somewhat noisy. Forces and torques

obtained using all three transformations are shown in black: thick lines are medians, while thin lines track individual realizations. Grey dotted lines show slopes of $-1/2$. Red, green, and blue lines show medians obtained using each of the three transformations separately; individual realizations are not shown to limit clutter.

Compared to the others, bulk forces on groups are relatively *insensitive* to averaging. For $N_{\text{avg}} \geq 128$, the force on each of the five group realizations converges toward a nonzero value specific to that particular system's layout. Averaging is somewhat more effective at reducing torques, but here too the results appear to level off as N_{avg} increases. It seems that bulk forces and torques on groups *do not vanish*, no matter how many tree CSs are averaged over.

At first glance, this may seem surprising. Averaging *should* restore rotational and translational invariance; how can these group models still be subject to bulk forces? The answer, ultimately, goes back to Hernquist's (1987) observation that a particle and a distant cell don't exert equal and opposite forces; again, this is true regardless of the tree CS, so averaging doesn't mitigate it. A symmetric mass distribution induces a symmetric pattern of averaged force errors, so bulk forces effectively cancel out. But the group models are too asymmetric for this to happen (see Fig. 20); instead, residual forces can add coherently. The bulk torques on the groups presumably arise in much the same way.

Bulk forces and torques on the spherical and disc models track $\bar{F}_{\text{bulk}} \propto N_{\text{avg}}^{-1/2}$ and $\bar{T}_{\text{bulk}} \propto N_{\text{avg}}^{-1/2}$ *remarkably* well. These models have highly symmetric mass distributions, so residual forces can

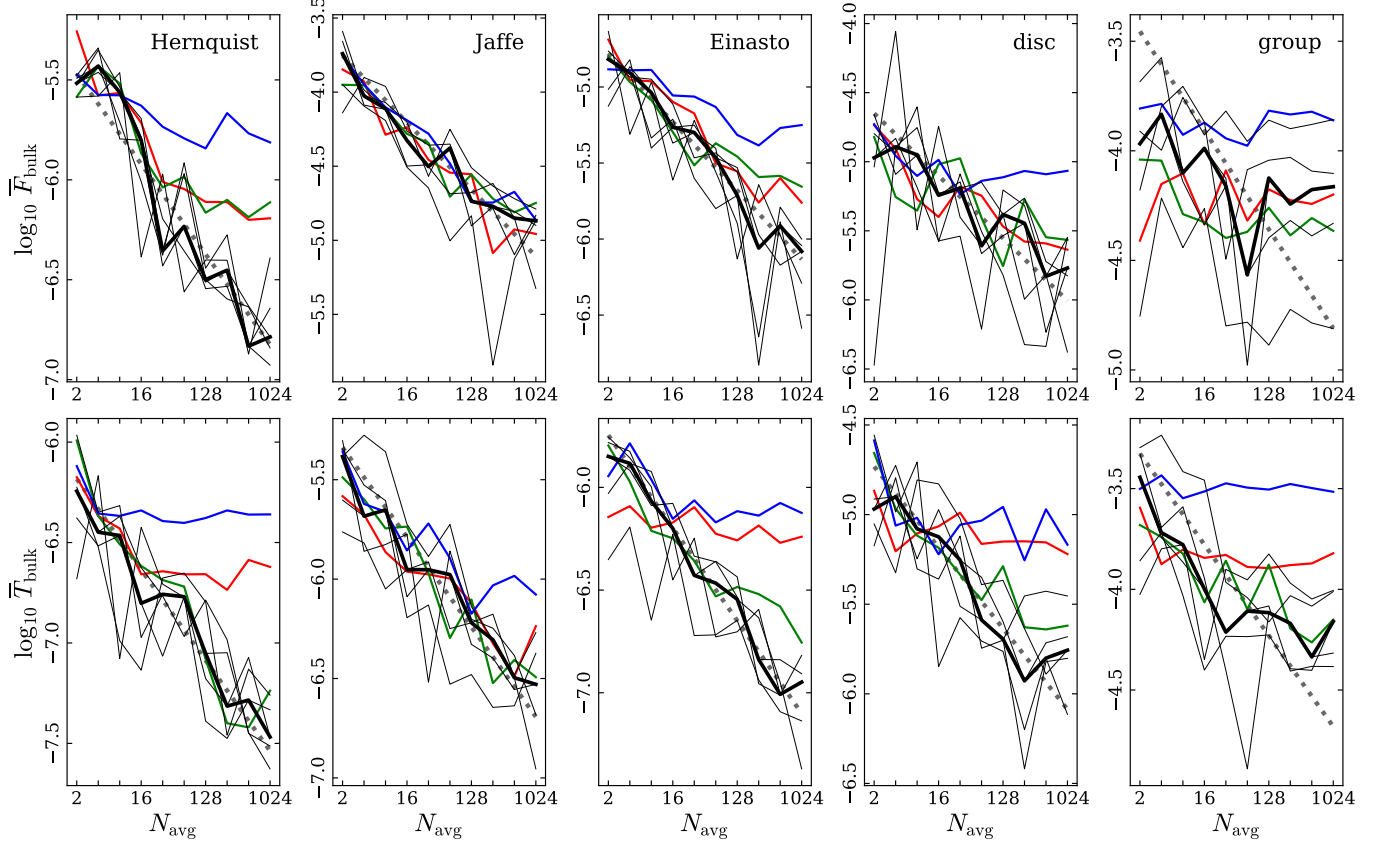


Figure 19. Tree-averaged bulk forces (top) and torques (bottom) vs. number of averages. Plotting conventions follow Fig. 17, however, individual realizations (thin lines) are only shown for all three transformations together to reduce crowding and confusion.

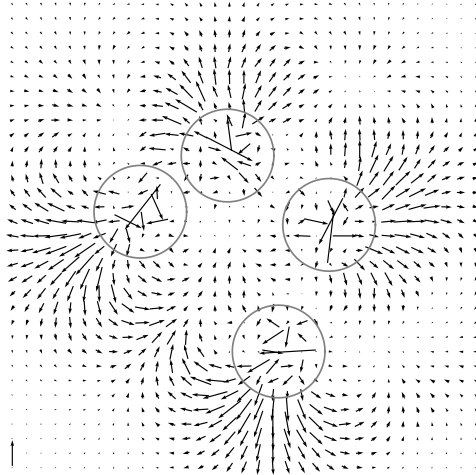


Figure 20. Residual acceleration errors for a planar group. All four Einasto models lie in the same plane, viewed face-on. Forces computed with $\theta = 0.8$ were averaged over $N_{\text{avg}} = 256$ CSs. Unit circles show positions and half-mass radii of group members. The vertical arrow at the lower left shows an acceleration error $|\Delta\bar{\mathbf{a}}| = 0.0003$.

cel almost perfectly. Of course, any realization constructed with a finite number of particles has irregularities which weakly violate these symmetries. Thus at some point, forces and torques on these realizations should peel away from the $N_{\text{avg}}^{-1/2}$ scaling law, and even-

tually level, off much as the group models do. Bulk forces on the Jaffe realizations do appear to be leveling off for $N_{\text{avg}} \geq 512$. The discs may also be reaching the limits of their $N_{\text{avg}}^{-1/2}$ scaling, again because of fluctuations due to finite N . Realizations with more particles should track $N_{\text{avg}}^{-1/2}$ scaling even better than the examples shown here; unfortunately, testing this is expensive!

In passing, it's striking that bulk forces and torques on the spherical and disc models follow $N_{\text{avg}}^{-1/2}$ scaling well beyond the point where the acceleration errors for these models (Fig. 17) are clearly leveling off. This illustrates the point that bulk forces and torques encode information above and beyond RMS acceleration errors.

Fig. 19 also uses red, green, and blue lines to show how bulk forces and torques respond to averaging using each transformation separately: red for translation, green for rotation, and blue for scaling. For the spherical and disc models, rotation and translation appear about equally effective at mitigating bulk forces. Naively, one might expect that bulk forces should respond more to translation than to rotation. A likely explanation of the actual results is that by potentially displacing a realization's centre to any point on a sphere of radius r_{off} , rotation provides benefits similar to translation. Conversely, rotation is usually superior to translation at mitigating torques; the exception is the Jaffe model, which seems to benefit about equally from both transformations.

Fig. 21 shows how bulk forces and torques, averaged over $N_{\text{avg}} = 256$ tree CSs, depend on opening angle. Comparison with Figs. 10 and 12 again confirms that averaging and opening angle work well together. Bulk forces and torques on spherical and disc models are

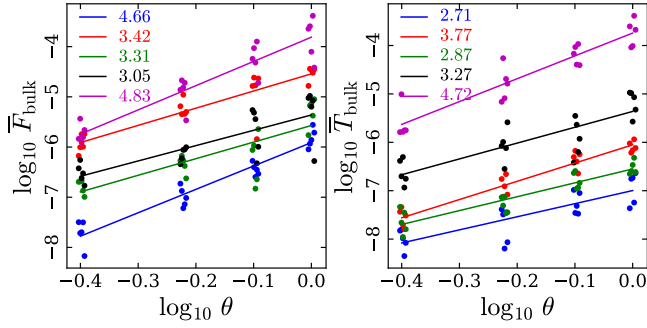


Figure 21. Bulk forces and torques vs. opening angle, obtained by averaging over $N_{\text{avg}} = 256$ tree CSs. Compare with Figs. 10 and 12.

reduced by an order of magnitude. Due to their intrinsic asymmetry, groups benefit somewhat less, but their bulk forces and torques fall off rapidly as θ decreases.

5 DISCUSSION

Tree averaging is an example of a general strategy in numerical calculation: *don't reuse a single approximation* if alternatives exist. An oct-tree provides a convenient set of approximations for evaluating gravitational forces, but if the tree is always built using the same CS, the same approximations will be used again and again. Randomizing over a plurality of tree CSs breaks this repetitive pattern, delivering more accurate results. For highly symmetric systems, accelerations computed by averaging can be an order of magnitude more accurate than those obtained from a single CS. The gains for asymmetric systems (i.e., groups) are somewhat smaller but still significant. In addition, averaging makes tree-codes more accurately invariant under translations and rotations.

Yet averaging is not a universal panacea: once the accidental errors arising from a specific choice of tree CS have been suppressed, a different category of error, intrinsic to *any* hierarchical force calculation scheme, comes to light. In particular, averaging does not address the fact that highly flattened or stratified mass distributions generate cells with large octapole-plus moments, or prevent an array of such cells, all sampling the same mass distribution, from producing correlated errors. Nor does averaging resolve the asymmetry between a cell c acting on a particle p and a particle p acting on the particles $p' \in c$ (Hernquist 1987); thus averaged force calculations can still yield nonzero bulk forces and torques unless interactions are explicitly symmetrized (Dehnen 2000; Marcello 2017; Korobkin et al. 2021).

The relationship between momentum conservation and galilean invariance is straightforward if forces are conservative: Noether's theorem shows that conservation laws are consequences of invariance. But Fig. 16 demonstrates that forces averaged over multiple tree CSs are *not conservative*. Thus a tree-code may approach invariance but not conserve momentum; the unequal forces a particle and a cell exert on each other are still in effect. For example, a configuration consisting of a Gaussian sphere and a thin disc, separated by 2 length units along the minor axis of the latter, reliably generates a strong bulk force toward the sphere; after averaging, this force is independent of the system's position or orientation, demonstrating translational and rotational invariance.

Lagrangian tree-codes using trees constructed via a nearest-neighbor scheme (Benz et al. 1990) might seem to have an advantage

here; the tree is already invariant under translation, rotation, and scaling. However, this built-in invariance still permits violations of Newton's third law. Moreover, it's not clear how to incorporate other benefits of averaging; each particle configuration generates a *unique* tree, in contrast to the plethora of trees an Eulerian codes can generate via an affine transformation (eq. 2). Is it worth introducing randomness into a nearest-neighbor tree to decorrelate errors?

The idea behind averaging is very general, and it may be useful for a wide variety of codes. Any tree, adaptive refinement, or mesh code which implements vacuum boundary conditions (BC), typically employed for simulations of isolated systems (including encounters), could use rotation and translation with little difficulty; scaling is problematic for codes with mesh-based resolution. The advantages may depend on the type of code; e.g., Cartesian mesh codes may benefit from rotation, since they don't conserve angular momentum accurately (Hernquist 1987).

Tree-codes implementing periodic BCs via Ewald summation can't use random rotation; the rotated field density field does not preserve periodic BCs. Scaling is precluded, since the root cell must be identified with the simulation volume. But translation is relatively straightforward; Springel et al. (2021) describe a code which does exactly that, optionally in conjunction with a momentum-conserving force calculation algorithm (Dehnen 2000). On the other hand, periodic-BC codes which use a particle-mesh algorithm to handle long-range forces and a tree-code to 'fill in' short-range forces (Xu 1995; Bagla 2002; Springel 2005) are *effectively* using the latter to solve a vacuum-BC problem, and may be able to deploy all three transformations.

The averaging procedure described here chooses tree CSs at random. Is this the best strategy? Random sampling spans the entire space of possibilities, but not efficiently. Iterating over a well-chosen sequence of tree CSs might be better, much as panel integration is typically more accurate than Monte-Carlo integration. However, choosing the CS sequence seems non-trivial; it may depend on both the system to be simulated and the specific objectives of the simulation. On the other hand, randomness is easy to implement and minimizes a priori assumptions.

Likewise, the opening criteria in § 2.3 minimize a priori assumptions, basically aiming to constrain the relative error of each cell. Conversely, GADGET (Springel, Yoshida, & White 2001) prioritizes the accuracy of the cells which exert the largest forces. This seems reasonable, and is very likely to reduce the broad spread of acceleration errors shown in the lower right panel of Fig. 2, but it builds in some assumptions about simulation objectives. As an alternative, it may be useful to reduce θ for cells with large octapole-plus moments, identified either by explicit calculation or by heuristics (e.g., standard deviation of mass in descendent nodes).

6 CONCLUSIONS

A single oct-tree provides a representation of an N -body mass distribution which can be used to compute approximate gravitational forces. Averaging over a *plurality of representations* partly cancels errors and thereby improves the results of these computations, while revealing a substratum of more fundamental errors.

The tree-code described in this paper implements averaging. I characterize the code's performance in detail, aiming to demonstrate limitations as well as advantages. § 2 presents the algorithm; the main innovation is simply to apply a random angle-preserving affine transformation to particle coordinates before constructing the tree.

This offers no advantages for a single force calculation; rather, the advantages accrue over multiple force calculations.

The systematics of tree-code force calculation are explored in § 3. A key point, which emerges early, is that force-calculation errors are correlated at several levels. First of all, the forces that different cells exert on a given particle have errors which are not statistically independent. Second, adjacent particles typically interact with similar sets of cells, and consequently may have have similar force-calculation errors.

§ 4 examines the results of averaging over tree CSs. Averaging suppresses errors which depend on the position and orientation of the root cell, improving the accuracy of potentials and accelerations and substantially reducing bulk forces and torques. On the other hand, errors which are independent of the tree CS are immune to averaging. For example, discs give rise to larger force errors because they are represented by trees containing cells with large octapole moments; averaging improves disc forces but exposes an eightfold pattern of errors (Fig. 16) which are likely intrinsic to any tree code using quadrupole but not octapole moments.

In any case, averaging over multiple tree CSs is an inefficient way to improve force calculations for *static* systems. The CPU time is proportional to the number of averages, so errors scale like $t_{\text{cpu}}^{-1/2}$ at best. In contrast, changing θ yields errors which scale roughly as $t_{\text{cpu}}^{1.4}$. For static systems, averaging restores rotational and translational invariance, but at a very high cost. Rather, the idea is to implement averaging in dynamical simulations by using a different tree CS for each time-step. However, it's not a given that randomizing tree CSs *while particles move* will work as well as it does for static configurations. The next paper will examine how tree averaging performs in various dynamic simulations; some preliminary results appear below.

6.1 Preliminary Dynamical Tests

Quantifying the accuracy of an N -body simulation is problematic, since we lack reference solutions for $N > 2$ particles. However, simulations which conserve energy, momentum, and angular momentum within narrow tolerances are generally preferable to those which do not.

Fig. 22 (top panel) shows that averaging can improve energy conservation by an order of magnitude in simulations of spherical systems. Here, energy conservation is gauged by $\delta E \equiv (E(t) - E(0))/|E(0)|$, where $E(t)$ is the net binding energy⁷. Eight Hernquist models, each containing $N = 2^{18}$ particles, were each run for ~ 15 half-mass orbital periods, using a time-step $\Delta t = 1/256$, an opening angle $\theta = 1$, and a softening length $\epsilon = 0.01$. Solid and dotted lines show results for averaged-tree and fixed-tree simulations, respectively.

The large differences between the runs with and without averaging strongly implicates force calculation as the main driver of these energy conservation errors. Other tests (not shown) indicate that errors due to the time-step or numerical precision (32-bit floating-point) set a floor on $|\delta E|$ at least an factor of ten *below* the best outcomes shown here. It may be appropriate to think of these force errors as an external ‘heat source’ driving the net binding energy E upward toward zero. It’s worth noting that the errors at each time-step are comparable in all eight simulations; in the averaged runs, these

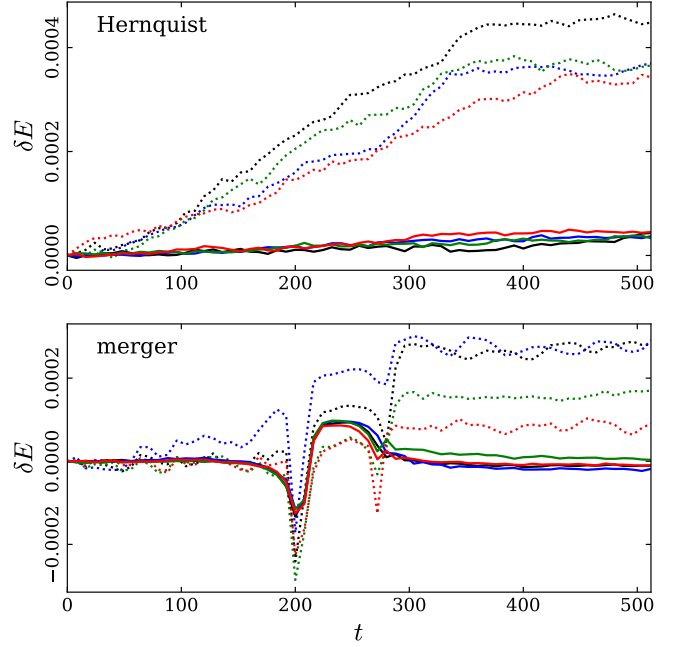


Figure 22. Relative energy conservation errors vs. simulation time for (top) isolated Hernquist models and (bottom) parabolic mergers of Hernquist models. Solid and dotted lines show results with and without averaging, respectively; colors simply distinguish realizations.

errors have less effect because they are decorrelated correlated from one time-step to the next.

(Parenthetically, it’s curious that the un-averaged runs seem to level off as they approach $\delta E \simeq 0.0004$. Why this happens is unclear; there’s no obvious structural change which could moderate the effects of force errors toward the end of these runs. The variation among these experiments also lacks explanation. Further examination of these points is beyond this paper’s scope.)

Mergers of equal-mass systems are represented in the bottom panel of Fig. 22. Eight pairs of isotropic Hernquist models were placed on inbound parabolic orbits reaching pericentres $r_{\text{peri}} = 2$ length units apart at $t_{\text{peri}} \simeq 200$ time units (Saleh & Barnes 2024). These runs used the modified treecode (Appendix A), with $N = 2^{18}$ particles, $\Delta t = 1/256$, $\theta = 0.8$, and $\epsilon = 0.01$. Again, averaged and fixed-tree simulations are represented by solid and dotted lines.

As above, averaging improves energy conservation, but now the picture is more complicated. In both the averaged and fixed-tree simulations, δE drops abruptly when the models first encounter each other ($t \simeq 200$), and rebounds as they separate; some of the fixed-tree simulations seem to repeat this pattern when the systems merge ($t \simeq 280$). The sign of this variation suggests that the net accelerations of the two models are slightly but systematically underestimated when they are close to each other; as a result, the models arrive at their first pericentric passage with slightly less kinetic energy than they should have.

Closer examination sharpens contrasts. The four averaged runs track each other *very* closely. The four runs without averaging, besides responding more strongly at first encounter, display large run-to-run variations; in particular, some of these simulations exhibit sporadic increases in δE , finally leveling off after the models merge. These variations, while comparable in magnitude to the gradual upward drift in δE seen in the top panel, probably have a different origin. In particular, the large run-to-run differences indicate that δE is

⁷ To estimate $E(t)$ more accurately, the gravitational energy was recalculated from particle snapshots saved every 8 time units using $\theta = 0.5$.

sensitive to the precise trajectories of the models with respect to the fixed tree structure. Averaging, by restoring translational invariance, mitigates such effects.

How significant are the conservation errors seen in Fig. 22? One natural scale is the overall variation in binding energy between statistically independent realizations, which in relative terms is $\delta E \sim N^{-1/2} \simeq 0.002$. This is a factor of 5 to 10 larger than any of the energy errors found here; by this standard, all of these experiments are fairly accurate.

But energy conservation is not the only standard. Conservation of angular momentum is critical in simulations of binary systems (Marcello 2017; Korobkin et al. 2021). For example, a 1 per cent change in the magnitude of the orbital angular momentum of a merging encounter yields a change of comparable magnitude in the time between first and second pericentres. The fixed-tree merger experiments violate orbital angular momentum conservation at the 0.1 per cent level, enough to contribute to run-to-run variations in merger time-scales (Saleh & Barnes 2024). In contrast, the four merger experiments with averaging conserve orbital angular momentum to one part in 10^4 or better.

ACKNOWLEDGMENTS

I thank Jeremy Goodman, Colby Haggerty, Lars Hernquist, Piet Hut, Jun Makino, Kegio Nitadori, Atsushi Taruya, and Simon White for helpful discussions, and the referee for a constructive report. I'm also grateful to Minghui Chen for reviving the decade-old hardware used for most of these experiments. Technical support and advanced computing resources from University of Hawai'i Information Technology Services – Research Cyberinfrastructure, funded in part by the National Science Foundation CC* awards # 2201428 and # 2232862, are gratefully acknowledged. Publication costs were covered by the Institute for Astronomy.

DATA AVAILABILITY

An open-source implementation of the simulation code is available at <https://github.com/barnes-astro/Treecode2>. Please direct requests for the test data and analysis code to the author, barnes@hawaii.edu.

REFERENCES

Aarseth, S. J., 1963, MNRAS, 126, 223
 Appel, A. W., 1981, PhD Thesis, Princeton Univ.
 Appel, A. W., 1985, SIAM J. Sci. Stat. Comput. Phys., 6, 85
 Bagla, J. S., 2002, J. Astrophys. Astr., 23, 185
 Barnes, J. E., 1990, J. Comp. Phys., 87, 161
 Barnes, J. E., 1994, in *The Formation and Evolution of Galaxies*, (Cambridge University Press)
 Barnes, J. E., 2012, MNRAS, 425, 1104
 Barnes, J., Hut, P., 1986, Nature, 324, 446
 Barnes, J. E., Hut, P., 1989, ApJS, 70, 389
 Benz, W., Bowers, R. L., Cameron, A. G. W., Press, W. H., 1990, ApJ, 348, 647
 Binney, J., Tremaine, S., 2008, *Galactic Dynamics: Second Edition*. Princeton University Press, Princeton, NJ
 Calleja, R., Doedel, E., García-Azpeitia, C., 2018, Cel. Mec. Dyn. Astr., 130, 48
 Dehnen, W., 2000, ApJ, 536, L39
 Einasto, J., 1965, Trudy Astrofizicheskogo Instituta Alma-Ata, 5, 87
 Greengard, L., 1990, Computers in Physics, 4, 142

Greengard, L., Rokhlin, V., 1987, SIAM J. Sci. Stat. Comput., 9, 669
 Hernquist, L., 1987, ApJS, 64, 715
 Hernquist, L., 1990, ApJ, 356, 359
 Hernquist, L., Ostriker, J. P., 1992, ApJ, 386, 375
 Hockney, R. W., Eastwood, J. W., 1988, *Computer Simulation Using Particles*. Adam Hilger, Bristol
 Jaffe, W., 1983, MNRAS, 202, 995
 Jernigan, J. G., 1985, in IAU Symp. 113, ed. J. Goodman, P. Hut, 275
 Knuth, D., 1973, *Fundamental Algorithms*, Reading, Addison-Wesley
 Korobkin, O., Lim, H., Sagert, I., Loiseau, J., Mauney, C., Alexander, M., Kaltenborn, R., Tsao, B.-J., Even, W. P., 2021, arXiv:2107.07166v1
 Makino, J., 1990a, J. Comp. Phys., 87, 148
 Makino, J., 1990b, J. Comp. Phys., 88, 393
 Makino, J., 1991, PASJ, 43, 621
 Marcello, D. C., 2017, AJ, 154, 92
 McGlynn, T. A., 1984, ApJ, 281, 13
 Merritt, D., 1985, AJ, 90, 1027
 Osipkov, L. P., 1979, Azh, 5, 77L
 Plummer, H. C., 1911, MNRAS, 71, 460
 Porter, D., 1985, PhD Thesis, UC Berkeley
 Press, W. H., 1986, in *The Use of Supercomputers in Stellar Dynamics*, ed. P. Hut, S. McMillan, 184
 Saleh, L., Barnes, J. E., 2024, MNRAS, 527, 8551
 Salmon, J., Warren, M., 1994, J. Comp. Phys., 111, 136
 Springel, V., 2005, MNRAS, 364, 1105
 Springel, V., Yoshida, N., White, S. D. M., 2001, New Astronomy, 6, 79
 Springel, V., Pakmor, R., Zier, O., Reinecke, M., 2021, MNRAS, 506, 2871
 Stadel, J. G., 1992, PhD Thesis, U. Washington
 Toomre, A., 1964, ApJ, 139, 1217
 Wang, J., Bose, S., Frenk, C. S., Gao, L., Jenkins, A., Springel, V., White, S. D. M., 2020, Nature, 585, 39
 Xu, G., 1995, ApJS, 98, 355

APPENDIX A: MODIFIED TREE-CODE

Even with threading, scanning the tree is expensive. Algorithm 1 visits only $O(\log N)$ nodes to compute the force on a particle, but these nodes are scattered in memory and are accessed in random order. Moreover, the sequence of operations is hard to predict, thwarting many of the optimizations attempted by modern compilers.

Physically adjacent particles typically interact with very similar sets of nodes. This suggests a straight-forward way to reduce the number of tree scans (Barnes 1990): construct a list of interactions which applies everywhere within some small neighborhood, and reuse it for each particle contained therein. The ‘modified’ algorithm finds such neighborhoods by scanning the tree, looking for cells containing no more than n_{share} particles, where $n_{\text{share}} \sim 10^2$ is a user-specified parameter. Each time it finds a suitable cell c' , it lists the particles inside, and evaluates their mutual interactions. It then performs a single tree scan to find nodes outside c' with which all the particles in c' can interact, storing the relevant data in two arrays of particles and cells. These arrays are then used to sum the external field on each particle in c' ; everything is in a linear format, so memory access and instruction pipelining can be efficiently optimized. The linear organization of the data is also compatible with multi-threading, GPU execution, or specialized N -body hardware (Makino 1991).

The version of the algorithm presented here differs slightly from the earlier version (Barnes 1990). To decide if particles in c' could safely interact with cell c , the old version needed the minimum distance between the volumes represented by c' and c . That distance is easily evaluated in the tree’s CS, but harder to compute in simulation coordinates, making the *MustOpen* function more costly and explicitly dependent on details of tree construction. Instead, the new code employs an (almost) coordinate-free criterion. First, a sphere

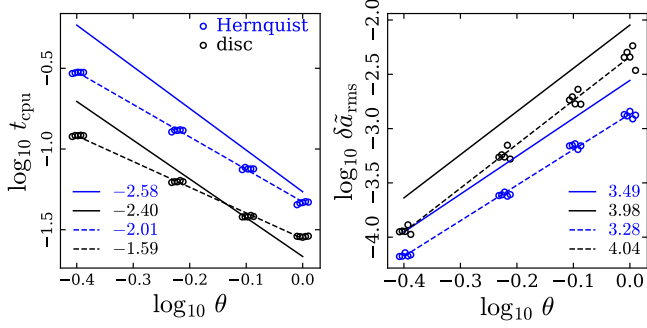


Figure A1. Modified tree-code (dashed lines, open circles) compared to standard tree-code (solid lines). Left: CPU time vs. opening angle. Right: acceleration error vs. opening angle. All tests used $N = 2^{18}$ particles; the modified code used $n_{\text{share}} = 64$.

which bounds the particles in c' is identified. This sphere is centred at \mathbf{r}_{mid} , which is found by averaging minimum and maximum particle positions along all three simulation coordinates; its radius r_{max} is the maximum distance of any particle in c' from \mathbf{r}_{mid} . Then, during the tree scan, a cell c at a distance $s = |\mathbf{r}_{\text{mid}} - \mathbf{r}_c|$ must be opened if

$$s < \ell_c/\theta + d_c + r_{\text{max}}. \quad (\text{A1})$$

This condition guarantees that every particle in c' can interact with c without falling afoul of eq. (9). For a given θ , it typically increases the number of particle-cell interactions computed by ~ 20 per cent, and the number of particle-particle interactions by a factor of a few. This somewhat improves the algorithm's accuracy. The effect on computing time will depend on the computing architecture employed; some specific results for a single-threaded implementation on a conventional CPU are briefly covered below.

An unintended side-effect of eq. (A1) is that *every* cell c within radius $s < r_{\text{max}}$ of \mathbf{r}_{mid} must be opened. In situations where c' is embedded in a steep, large-scale density gradient, this radius can extend beyond c' and enclose an absurdly large number of particles, which must be included in the external interaction list. Rather than allocating arrays large enough to deal with this very rare situation, the modified code aborts the tree walk if more than a fixed number of external particles and cells are found. In the event of an abort, the algorithm simply processes the immediate descendants of c' instead of c' itself. Since these cells are smaller than c' , their r_{max} radii are guaranteed to enclose fewer external particles, eventually resolving the problem. By default, space is allocated for a total of 20000 particles and cells, which is generous in light of typical usage; this allocation may be worth tuning if tree-walks are frequently aborted, which is more likely for calculations with smaller opening angles (e.g., $\theta \lesssim 0.4$).

Modified tree-code tests

The modified code avoids recursive tree scans in favor of iteration over linear arrays, which can be more easily optimized, vectorized, or parallelized. One simple gauge of the algorithm's performance is the average number of particles which share a list. This average is $\sim 0.28n_{\text{share}}$, with little sensitivity to the mass model, particle number for $N \geq 2^{18}$, or value of $n_{\text{share}} \in [16, 256]$.

Increasing n_{share} reduces the number of tree scans, but *increases* the number of nodes per average interaction list. At some point, the growing cost of summing over the interactions exceeds the saving afforded by fewer tree scans. The total cost per force calculation

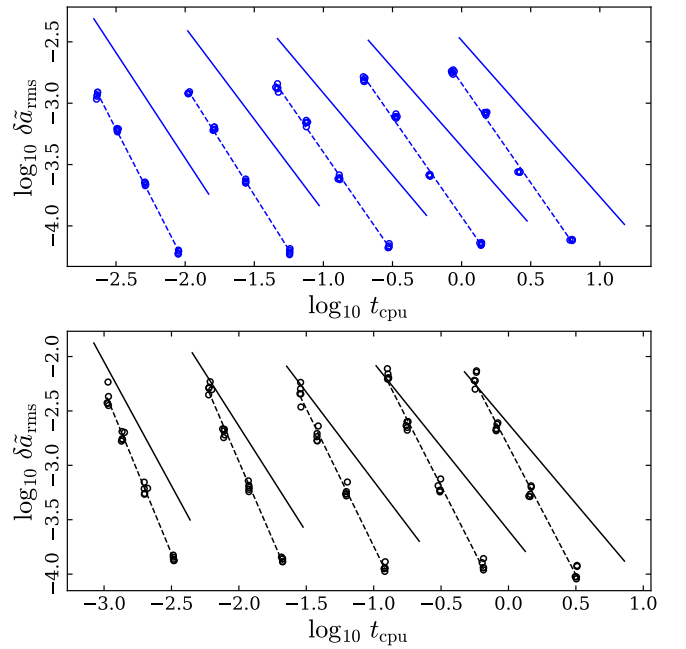


Figure A2. Acceleration error versus computing time for modified (open circles, dashed lines) and standard (solid lines) tree-codes. Open circles sample the relationship between t_{cpu} and $\delta\tilde{a}_{\text{rms}}$ for $\theta = 1.0, 0.8, 0.6, 0.4$; lines are fits. Five values of N , progressing from $N = 2^{14}$ (left) to $N = 2^{22}$ (right), are shown. Top panel plots Hernquist models, bottom panel shows disc models.

has a broad minimum for intermediate values of n_{share} . This optimal value for n_{share} depends on hardware and implementation details; for example, if the force summation is accelerated (e.g., by multi-threading or special-purpose hardware), the minimum CPU time will be reached for a larger n_{share} . Preliminary results for a single CPU-only system indicate $n_{\text{share}} \simeq 64$ is a good choice, with little sensitivity on other parameters.

In the left panel of Fig. A1, I compare CPU times for the single-thread implementation of the modified code and the standard version. The speed-up depends on the mass model and θ , and to some degree on the value of N as well. For the Hernquist model, the modified code is always faster, while for the disc model, the standard code is faster for $\theta < \theta_{\text{be}} \simeq 0.7$, but slower for smaller θ values. This break-even point shifts to $\theta_{\text{be}} \simeq 0.8$ (0.4), for $N = 2^{22}$ (2^{14}) particles.

Increasing the number of nodes on the interaction list also improves the accuracy of force calculations. This is shown on the right in Fig. A1, which plots RMS acceleration errors vs. θ for the same ensembles shown on the left. For any given θ value, the modified code is about twice as accurate as the standard one. Similar gains are realized for other mass models. This improvement results largely from better treatment of interactions on relatively short scales – a few times the diameter of the set of particles sharing an interaction list. As N increases, these short-range interactions provide a smaller fraction of the total force, and the gain in accuracy gradually decreases.

Although the modified code was originally developed to take advantage of vectorized or parallel architectures, it outperforms the standard code even on scalar CPUs. This is demonstrated in Fig. A2, which plots RMS force error vs. computing time. Each slanting line shows how these quantities vary for θ values within $[0.4, 1.0]$, holding the number of particles fixed. Solid and dashed lines represent the standard and modified code, respectively. The left-most pair of solid and dashed lines show results for $N = 2^{14}$ particles; each step to the

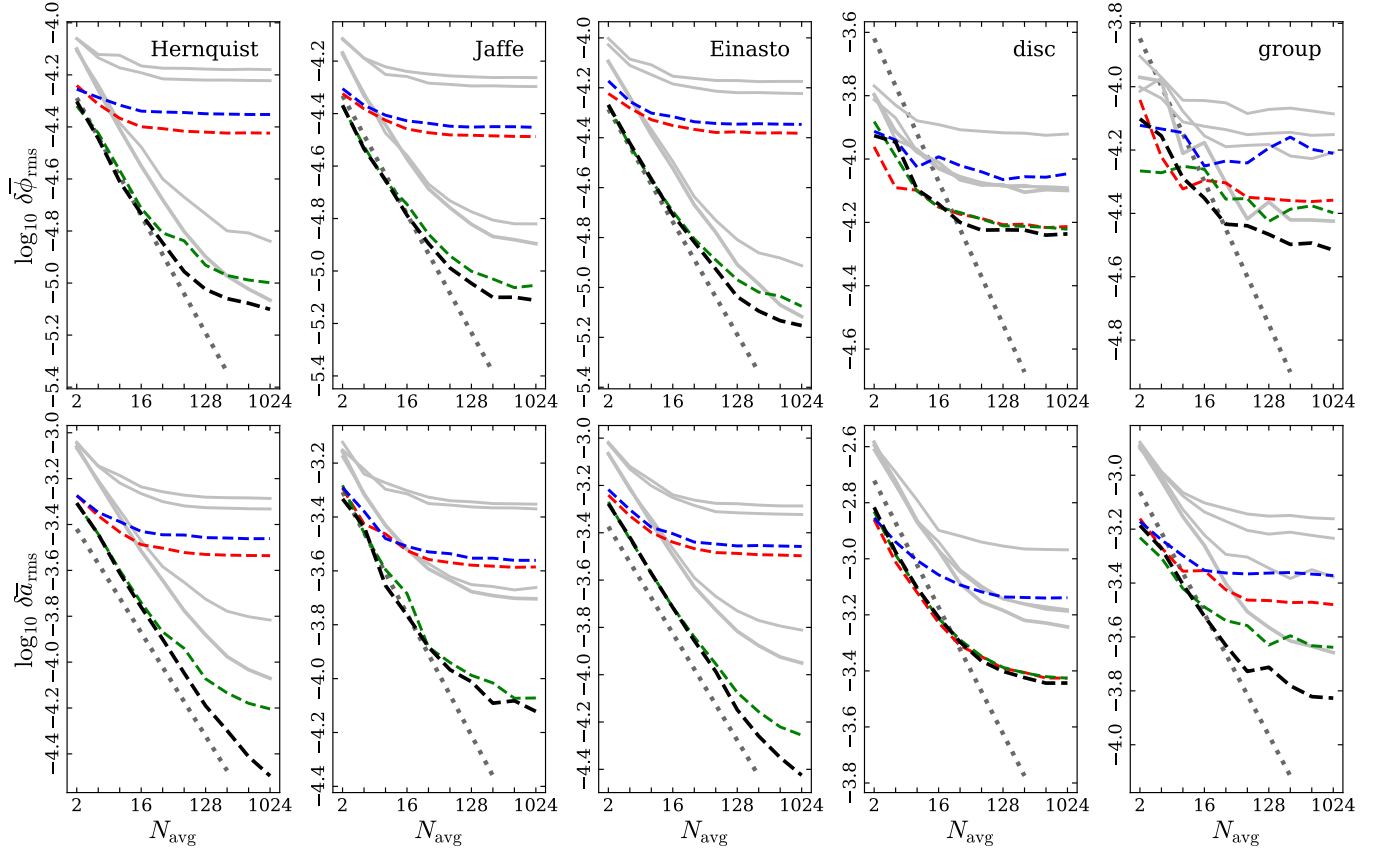


Figure A3. Dashed curves show RMS errors in tree-averaged potentials (top) and accelerations (bottom) vs. number of averages, computed using the modified code. Solid grey curves show corresponding results for the standard code from Fig. 17.

right represents a four-fold increase in N , up to $N = 2^{22}$ on the right. For any given level of accuracy, the modified code is faster, although the speedup is never much more than a factor of two, and approaches unity for disc models with large- N and $\theta = 1$. This modest speedup arises because the force-summation data is organized into linear arrays, which allow the compiler to generate more efficient code. Larger gains can be expected if force summations are parallelized or non-CPU hardware can be used.

Finally, is the modified code compatible with tree-averaging? Fig. A3 plots RMS errors in potential and acceleration versus number of averages. This figure's layout parallels Fig. 17. Dashed curves show modified tree-code results, to be compared with the solid grey curves presenting median results for the standard code. For any given number of averages N_{avg} , the modified-code yields consistently better results than those produced by the standard code. In addition, averaged accelerations for the spherical models track the $N_{\text{avg}}^{-1/2}$ trend better than their standard counterparts.

This paper has been typeset from a $\text{\TeX}/\text{\LaTeX}$ file prepared by the author.

Treecode2: The Power of Pluralism

Supplemental Figures

Joshua E. Barnes

February 9, 2026

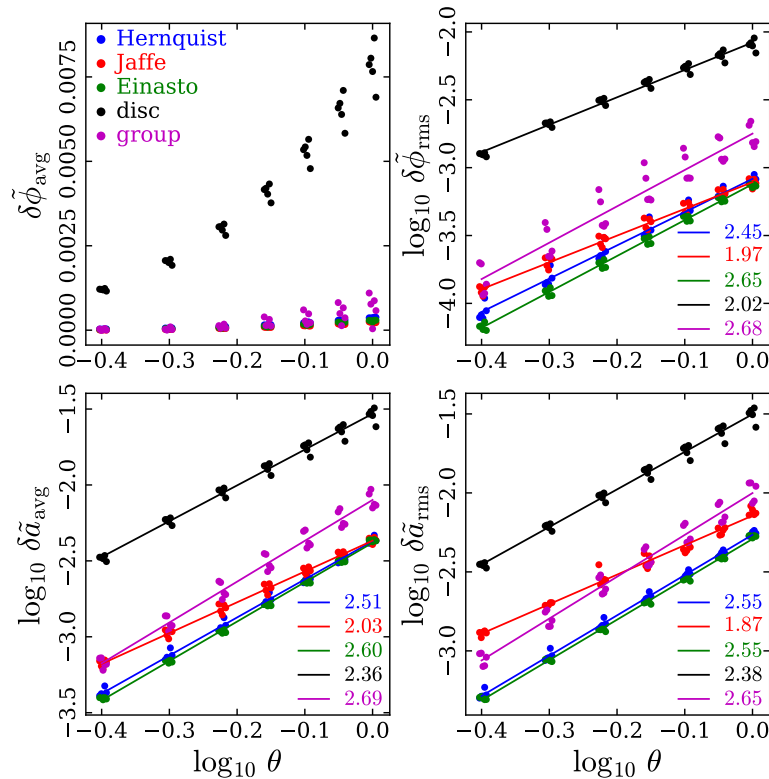


Figure 1: Similar to Fig. 6, but computed *without* quadrupole corrections.

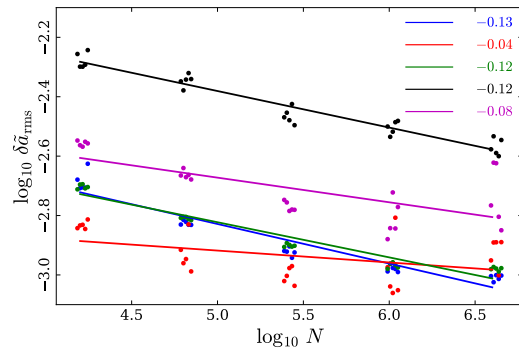


Figure 2: RMS acceleration errors, computed for $\theta = 0.8$, vs. number of particles. Color indicates mass model as in Fig. 6. Symbols show individual configurations, while lines are power-law fits with slopes as indicated.

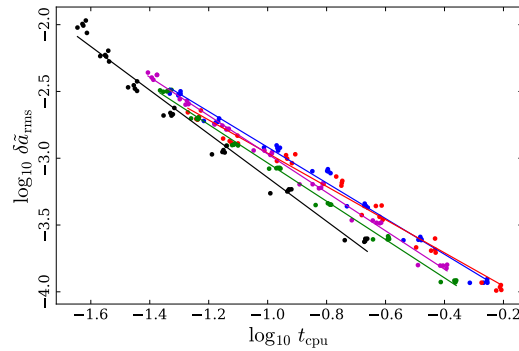


Figure 3: Acceleration error versus computing time.